

High-sensitivity millimeter imaging of molecular outflows in nine nearby high-mass star-forming regions

DE-JIAN LIU,^{1,2} YE XU,² YING-JIE LI,² SHENG ZHENG,¹ DENG-RONG LU,² CHAO-JIE HAO,^{2,3} ZE-HAO LIN,^{2,3}
SHUAI-BO BIAN,^{2,3} AND LI-MING LIU¹

¹ College of Science, China Three Gorges University, Yichang 443002, Peoples Republic of China;

² Purple Mountain Observatory, Chinese Academy of Sciences, Nanjing 210023, Peoples Republic of China;

³ School of Astronomy and Space Science, University of Science and Technology of China, Hefei 230026, Peoples Republic of China;

ABSTRACT

We present a study of molecular outflows using six molecular lines (including $^{12}\text{CO}/^{13}\text{CO}/\text{C}^{18}\text{O}/\text{HCO}^+$ ($J = 1 - 0$) and CS/SiO ($J = 2 - 1$)) toward nine nearby high-mass star-forming regions with accurate known distances. This work is based on the high-sensitivity observations obtained with the 14-m millimeter telescope of Purple Mountain Observatory Delingha (PMODLH) observatory. The detection rate of outflows (including ^{12}CO , ^{13}CO , HCO^+ , and CS) is 100%. However, the emission of SiO was not detected for all sources. The full line widths (ΔV) at 3σ above the baseline of these molecular lines have the relationship $\Delta V_{^{12}\text{CO}} > \Delta V_{\text{HCO}^+} > \Delta V_{\text{CS}} \approx \Delta V_{^{13}\text{CO}} > \Delta V_{\text{SiO}}$. ^{12}CO and HCO^+ can be used to trace relatively high-velocity outflows, while ^{13}CO and CS can be employed to trace relatively low-velocity outflows. The dynamical timescales of the ^{13}CO and CS outflows are longer than those of the ^{12}CO and HCO^+ outflows. The mechanical luminosities, masses, mass-loss rates and forces of all outflows (including ^{12}CO , ^{13}CO , HCO^+ , and CS) are correlated with the bolometric luminosities of their central IRAS sources.

Keywords: Jets (870), Interstellar clouds (834), Star formation (1569)

1. INTRODUCTION

The physical processes associated with low-mass star formation are reasonably well understood (e.g., Shu et al. 1987; McKee & Ostriker 2007; Kennicutt & Evans 2012). However, details of the forming mechanism(s) of high-mass stars remain poorly understood, so creating a clear map of high-mass star formation is extremely challenging work. To achieve this goal, it is vital to study molecular outflows, which arise during an important phase in high-mass star formation and are a ubiquitous phenomenon during the earliest stage of formation for stars of all masses (Beuther et al. 2002; Arce et al. 2007).

Since molecular outflows were first detected in Orion KL by Kwan & Scoville (1976), outflows in high-mass star-forming regions (HMSFRs) have been investigated by many researchers (Shepherd & Churchwell 1996; Zhang et al. 2001, 2005; Xu et al. 2006b; Li et al. 2018, 2019). In each of these studies, typically only one outflow tracer was used. However, there is no perfect outflow tracer, and a complete characterization of outflow phenomena requires observations made with many tracers (Bally 2016). Hence, to provide a more comprehensive understanding of the physical properties of outflows, it is necessary to conduct systematic studies of different molecular outflows using multiple molecular tracers toward HMSFRs.

Accurate distances over a relatively narrow distance range are important to statistically analyze the physical properties of outflows. Typical selection criteria in terms of distance have been commonly used: (1) the distances are measured by the trigonometric parallaxes of masers, which are typically more accurate than kinematic distances (Xu et al. 2006a; Reid et al. 2019), so more accurate physical quantities can be ascertained; (2) the sources are nearby and within a relatively narrow distance range (i.e., 0.5–1 kpc). In the context of PMODLH, the linear resolution can be

Table 1. List of objects.

ID	IRAS Name	Other Name	R.A.(J2000)	Decl.(J2000)	Dist (kpc)	Ref(s)
(1)	(2)	(3)	(4)	(5)	(6)	(7)
1	00338+6312	L1287	00:36:47.4	63:29:02	0.9	1
2	05345+3157	G176.51+00.20	05:37:52.1	32:00:03	1.0	2
3	06053-0622	Mon R2	06:07:47.9	-06:22:56	0.8	2, 3
4	06384+0932	NGC2264	06:41:09.9	09:29:14	0.7	4, 5
5	21007+4951	G090.21+02.32	21:02:22.7	50:03:08	0.7	6
6	21418+6552	G105.41+09.87	21:43:06.5	66:06:55	0.9	3, 6
7	22198+6336	...	22:21:26.7	63:51:37	0.8	7
8	22272+6358 A	L1206	22:28:51.4	64:13:41	0.8	1
9	22543+6413	Cep A	22:56:18.1	62:01:49	0.7	3, 8

NOTE— (1) ID. (2) and (3) Source name(s). (4) and (5) Position of the source (R.A.: hh:mm:ss.s, Decl.: dd:mm:ss). (6): Distance to the source. (7): Parallax reference.

References—(1) Rygl et al. (2010); (2) Xu et al. (2016); (3) Plume et al. (1992); (4) Kamezaki et al. (2014); (5) Schreyer et al. (1997); (6) Xu et al. (2013); (7) Hirota et al. (2008); (8) Moscadelli et al. (2009)

better than 0.27 pc with beam size of $\sim 55''$. This resolution is usually sufficient to visually depict the morphology of outflows, where the typical length of an outflow is about 1 pc.

This work is the first high-sensitivity systematic research of outflows, which was conducted using six molecular lines (i.e., SiO ($J = 1 - 0$), CS ($J = 2 - 1$), HCO⁺ ($J = 1 - 0$), ¹²CO ($J = 1 - 0$), ¹³CO ($J = 1 - 0$), and C¹⁸O ($J = 1 - 0$)) towards nine nearby HMSFRs (see Table 1). SiO was used as a shock tracer and the dense cores were mapped with C¹⁸O. Meanwhile, the molecular outflows were imaged using ¹²CO, ¹³CO, HCO⁺, and CS, which were utilized to trace areas of different densities in HMSFRs. These lines were observed by the same telescope with high-sensitivity observations and binned to the same pixel scales, which allowed us to make direct comparisons between the different line tracers. Additionally, the high-sensitivity observations were helpful for unveiling high-velocity outflow gas.

The remainder of the paper is organized as follows. We present the observations and data-reduction techniques in Section 2. In Section 3, we summarize the detected outflows and calculate the relevant physical quantities and the relationships between them. Finally, a summary of our work is given in Section 4.

2. OBSERVATIONS

The observations of nine HMSFRs were carried out from July 2019 to May 2020 using the PMODLH 14-m millimeters-wavelength telescope. The detailed observations of the six molecular lines are: (1) ¹²CO ($J = 1 - 0$)(115.271 GHz), ¹³CO ($J = 1 - 0$)(110.201 GHz) and C¹⁸O ($J = 1 - 0$)(109.782 GHz) were simultaneously observed from July to November 2019; (2) SiO ($J = 2 - 1$)(86.847 GHz) was observed from August 2019 to January 2020; (3) HCO⁺ ($J = 1 - 0$)(89.189 GHz) was observed from November 2019 to February 2020; and (4) CS ($J = 2 - 1$)(97.981 GHz) was observed in May 2020. All lines were observed with the nine-beam Superconducting Spectroscopic Array Receiver system in the sideband separation mode (Shan et al. 2012), where the lines of SiO, ¹³CO, and C¹⁸O were in the lower sideband, and ¹²CO, HCO⁺, and CS were in the upper sideband.

The lines of SiO were obtained via the single pointing observation mode with integration times over 40 min. Other lines were observed with the on-the-fly (OTF) mode, using typical sample steps of $10''$ – $15''$. The OTF raw data were gridded in a FITS cube with a pixel size of $30''$ using the GILDAS software package.¹ The typical integration time for each position was about 15 min. Each fast Fourier transform (FFT) spectrometer with a bandwidth of 1 GHz

¹ <http://www.iram.fr/IRAMFR/GILDAS>

Table 2. Basic observation parameters at the observed frequencies.

No	Lines	T_{sys} (K)	η_{mb}	HPBW ($''$)	Velocity resolution (km s $^{-1}$)
(1)	(2)	(3)	(4)	(5)	(6)
1	^{12}CO	250-300	0.49	49	0.159
2	^{13}CO	150-200	0.54	51	0.166
3	C^{18}O	150-200	0.54	52	0.166
4	SiO	100-150	0.58	62	0.205
5	HCO^+	100-150	0.60	61	0.187
6	CS	120-170	0.67	55	0.212

NOTE— (1) No. (2) Molecular line. (3) Typical system temperature (T_{sys}). (4) Main beam efficiency (η_{mb}). (5) Half power beam width (HPBW). (6) Velocity resolution.

provided 16384 channels, producing a spectral resolution of 61 kHz. The parameters of the antenna and the velocity resolutions of the spectrometers are listed in Table 2.²

All results presented in this work are expressed as brightness temperatures, $T_R^* = T_A^*/\eta_{mb}$, where T_A^* is the antenna temperature and η_{mb} is the main beam efficiency, which are listed in Table 2. The main beam root-mean-square (RMS) noises of the molecular lines for all observed sources are listed in Table 3.

3. RESULTS

3.1. Emission Peak spectra

We successfully detected ^{12}CO , ^{13}CO , C^{18}O , HCO^+ , and CS emission from all sources; unfortunately, we did not detect SiO emission for all sources.

The basic parameters of the molecular lines at the respective emission peaks are listed in Table 4. Meanwhile, the molecular line profiles of the emission peak of C^{18}O for each source are shown in Figure 1. To select the most suitable sensitivity to achieve maximum telescope efficiency, the following tests were performed for the CS observation of Cep A. When the integration time of each position was about 15 min, the RMS noise was about 15.9 mK, and the full width (ΔV) at 3σ above the baseline was 16.8 km s $^{-1}$. Then we doubled the integration time (i.e., to 30 min), finding an RMS noise of about 10.2 mK, and a full width of 17.7 km s $^{-1}$. There was no significant extension of its full width. Hence, we chose 15 min as the typical integration time of each position. Our results indicate the following relationship: $\Delta V_{^{12}\text{CO}} > \Delta V_{\text{HCO}^+} > \Delta V_{\text{CS}} \approx \Delta V_{^{13}\text{CO}} > \Delta V_{^{18}\text{O}}$. Meanwhile, multiple velocity features were visible in some line profiles, particularly those of ^{12}CO and HCO^+ , while ^{13}CO , C^{18}O , and CS were quite smooth.

SiO emission, which was used as a shock tracer, was not detected for all sources (see Figure 2). These sources had also been observed by Harju et al. (1998), who attempted to correlate the SiO emission with maser characteristics and with ultra-compact (UC) H_{II} regions. In their work, Harju et al. (1998) used the 15-m telescope Swedish-ESO Submillimetre Telescope (SEST) and the 20-m radio telescope of the Onsala Space Observatory in Sweden. Of the nine sources considered here, Harju et al. (1998) only detected SiO emission for L1287 with Onsala, whose velocity resolution was 0.17 km s $^{-1}$ and RMS was 20 mK, which were similar to what we achieved with our observations. Thus, the velocity resolution and sensitivity of PMODLH might not be the reason why we did not detect any SiO emission from L1287. Whilst the half power beam width (HPBW) of Onsala (i.e., 43 $''$) was better than that of PMODLH (i.e., 62 $''$). Harju et al. (1998) pointed out that SiO emission can be better traced by telescopes with higher resolutions (e.g. a 30-m telescope, which has a larger aperture). Therefore, resolution might be the reason why we did not detect SiO emission for all sources.

² <http://www.radioast.nsd.ccn/english/zhuangtaibaogao.php>

Table 3. Main beam RMS noise.

Source	RMS Noise (mK)					
	SiO	CS	HCO ⁺	¹² CO	¹³ CO	C ¹⁸ O
(1)	(2)	(3)	(4)	(5)	(6)	(7)
L1287	14.3	15.1	16.9	51.2	29.8	28.1
G176.51+00.20	18.1	15.3	17.2	60.9	32.8	31.5
Mon R2	15.3	15.6	18.3	51.1	25.7	24.2
NGC2264	14.5	16.1	16.3	47.4	27.5	25.9
G090.21+02.32	16.8	13.4	17.7	66.9	36.4	32.8
G105.41+09.87	17.8	13.2	17.2	50.0	27.5	27.0
IRAS 22198+6336	16.4	14.7	13.5	44.0	23.7	26.1
L1206	14.8	16.7	17.9	43.6	27.4	25.8
Cep A	15.3	10.2	21.4	50.8	32.0	29.4

NOTE— (1) Source name. (2), (3), (4), (5), (6) and (7) RMS noise of SiO, CS, HCO⁺, ¹²CO, ¹³CO, and C¹⁸O, respectively.

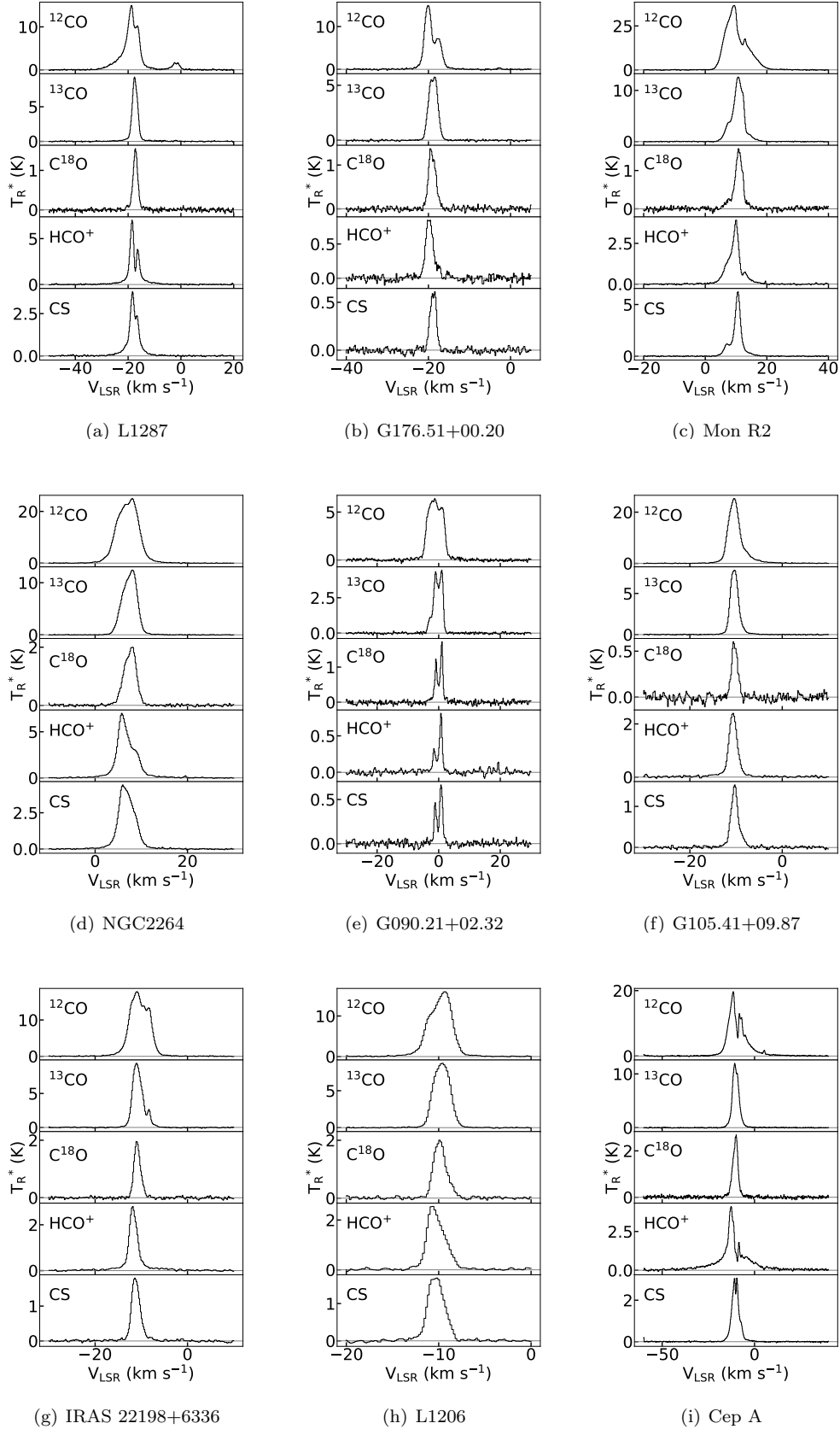


Figure 1. Line profiles of the molecular transitions for the nine HMSFR sources. The spectra were obtained at the position of the C^{18}O emission peak. The name of each source is given at the bottom of each panel. From top to bottom the lines are ^{12}CO , ^{13}CO , C^{18}O , HCO^+ , and CS .

Table 4. Basic parameters of the molecular lines.

Source	^{12}CO			^{13}CO			C^{18}O			HCO^+			CS		
	T_{R}^* (K)	V_{peak} (km s^{-1})	ΔV (km s^{-1})	T_{R}^* (K)	V_{peak} (km s^{-1})	ΔV (km s^{-1})	T_{R}^* (K)	V_{peak} (km s^{-1})	ΔV (km s^{-1})	T_{R}^* (K)	V_{peak} (km s^{-1})	ΔV (km s^{-1})	T_{R}^* (K)	V_{peak} (km s^{-1})	ΔV (km s^{-1})
(1)	(2)	(3)	(4)	(5)	(6)	(7)	(8)	(9)	(10)	(11)	(12)	(13)	(14)	(15)	(16)
L1287	19.0	-18.6	31.8	9.3	-17.6	11.6	1.6	-17.2	3.3	7.0	-18.5	17.4	3.8	-18.2	16.8
G176.51+00.20	14.9	-17.5	22.2	8.3	-19.2	5.8	1.4	-19.5	3.3	3.2	-18.1	18.5	3.2	-18.2	7.5
Mon R2	36.0	9.5	20.6	13.0	10.8	14.1	1.6	10.8	8.3	5.9	9.3	18.5	6.2	10.8	12.1
NGC2264	24.7	7.4	23.8	12.4	8.3	9.1	3.5	8.2	5.8	7.6	8.9	18.5	5.3	7.7	14.0
G090.21+02.32	8.0	0.6	15.9	5.1	0.9	6.7	1.7	1.2	5.0	1.4	0.7	4.1	0.8	1.0	2.8
G105.41+09.87	14.5	-11.3	17.5	9.9	-10.0	9.1	2.8	-9.2	2.5	3.7	-10.6	16.4	1.8	-10.1	6.5
IRAS 22198+6336	17.4	-11.0	15.9	9.3	-10.5	7.5	2.0	-11.0	3.3	2.8	-11.7	11.3	1.9	-11.6	6.5
L1206	17.0	-9.2	23.3	8.7	-9.5	5.0	2.0	-9.8	2.5	2.5	-10.7	5.1	1.7	-10.1	4.7
Cep A	22.4	-11.7	43.7	14.0	-11.6	16.6	2.7	-9.8	9.2	5.1	-12.4	47.2	3.5	-11.0	17.7

NOTE— (1) Source name. (2), (5), (8), (11) and (14) Brightness temperature(s) of the emission peaks of ^{12}CO , ^{13}CO , C^{18}O , HCO^+ , and CS, respectively. (3), (6), (9), (12) and (15) Central velocities of ^{12}CO , ^{13}CO , C^{18}O , HCO^+ , and CS, respectively. (4), (7), (10), (13) and (16) Full line width at 3σ above the baseline of ^{12}CO , ^{13}CO , C^{18}O , HCO^+ , and CS, respectively.

Table 5. Outflow parameters.

Source	^{12}CO		^{13}CO		HCO^+		CS	
	Δv_b (km s $^{-1}$)	Δv_t (km s $^{-1}$)	Δv_b (km s $^{-1}$)	Δv_t (km s $^{-1}$)	Δv_b (km s $^{-1}$)	Δv_t (km s $^{-1}$)	Δv_b (km s $^{-1}$)	Δv_t (km s $^{-1}$)
(1)	(2)	(3)	(4)	(5)	(6)	(7)	(8)	(9)
L1287	(-34, -21)	(-15, -8)	(-30, -20)	(-15, -6)	(-33, -20)	(-15, -6)	(-31, -20)	(-15, -6)
G176.51+00.20	(-47, -22)	(-15, -1)	(-25, -22)	(-16, -11)	(-39, -21)	(-16, 3)	(-27, -21)	(-15, -8)
Mon R2	(-2, 6)	(14, 30)	(4, 7)	(16, 21)	(0, 6)	(15, 22)	(-2, 4)	(17, 21)
NGC 2264	(-7, 0)	(12, 22)	...	(11, 15)	(-4, 4)	(12, 21)	(-5, 3)	(11, 17)
G090.21+02.32	...	(4, 12)	...	(2, 5)	...	(2, 7)	...	(2, 5)
G105.41+09.87	(-20, -13)	(-6, 3)	(-14, -12)	(-8, -5)	(-20, -13)	(0, 9)	(-15, -12)	(-8, -2)
IRAS 22198+6336	(-25, -15)	(-5, 0)	(-16, -13)	...	(-23, -14)	(6, 0)	(-16, -13)	(-9, -7)
L1206	(-21, -13)	(-7, -4)	(-13, -11)	(-8, -5)	(-24, -12)	(-8, -4)	(-16, -12)	(-9, -7)
Cep A	(-42, -21)	(-1, 33)	(-21, -15)	(-7, -3)	(-49, -21)	(-1, 27)	(-19, -15)	(-6, 1)

NOTE— (1) Source name. (2)–(9) Outflow velocity ranges (Δv) for the blue and red wings of ^{12}CO , ^{13}CO , HCO^+ , and CS, respectively.

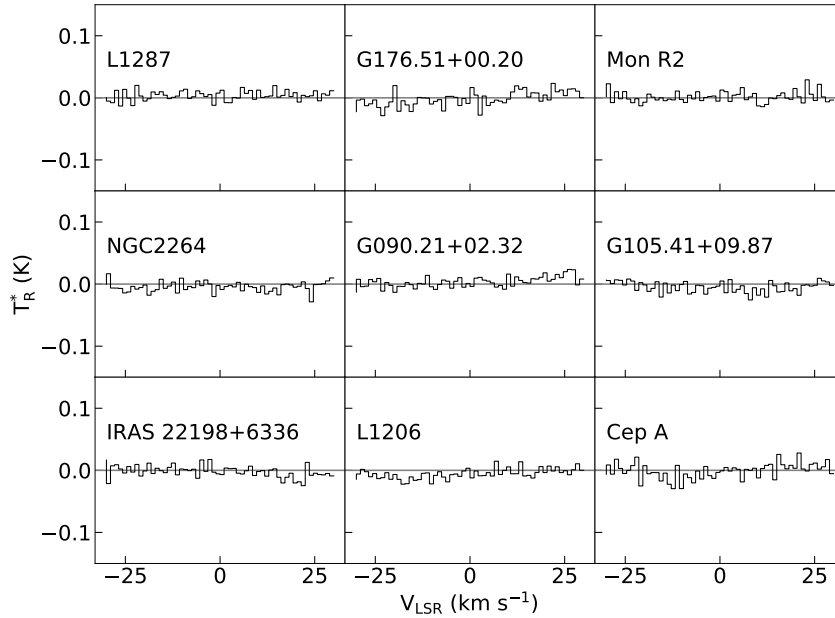


Figure 2. SiO spectra of the nine sources, including null detections. The name of each source is given in the top left-hand corner of each panel.

3.2. Outflow morphology

This work represents the first time that four molecular outflow tracers have been used in a single work (^{12}CO , ^{13}CO , HCO^+ , and CS), in addition to one shock tracer (SiO) and one dense core tracer (C^{18}O). With our observations, we successfully detected outflows associated with all nine sources. The high detection rate of outflows suggests that ^{12}CO , ^{13}CO , HCO^+ , and CS may be all suitably used to trace the molecular outflows of HMSFRs.

Outflow maps are presented in Figures 3–11. Within these figures, we have plotted the ^{12}CO , ^{13}CO , HCO^+ , and CS contours overlaid on the C^{18}O integrated images and WISE false-color images (Wright et al. 2010),³ where blue, green, and red correspond to the 4.6, 12, and 22 μm data, respectively. To determine the possible excitation sources of these outflows, we also marked the positions of the associated IRAS sources in the images, which were obtained from the IRAS Point Source Catalog 2.1.⁴ The bolometric luminosities of these IRAS sources were sourced from Sanders & Mirabel (1996). Meanwhile, the plotted spectra which have been smoothed to $5\delta v$ (i.e., we smoothed the data by merging five channels into a one channel) at the emission peaks of the blue and red lobes, and marked out the velocity ranges of the outflows using different color shades (see Figure 3 for details). The velocity ranges of the different outflows are listed in Table 5. Our main results are summarized as follows:

- ^{12}CO molecular outflows were detected for all sources. Eight sources (L1287, G176.51+00.20, Mon R2, NGC2264, G105.41+09.87, IRAS 22198+6336, L1206, and Cep A) showed clear bipolar or multiple outflow structures. Among them, the outflow of IRAS 22198+6336 was mapped for the first time, and NGC2264 was found to contain bipolar outflows for the first time. G090.21+02.32 appeared to show only a red lobe, although the source had been previously identified as a bipolar outflow (Clark 1986). The velocity ranges of the outflows of four sources (L1287, G176.51+00.20, Mon R2, and Cep A) have been extended with the improved high-sensitivity observations.

- We detected ^{13}CO molecular outflows for the first time for all sources. Six sources (L1287, G176.51+00.20, Mon R2, G105.41+09.87, L1206, and Cep A) showed clear bipolar or multiple outflow structures. Three sources (NGC2264, G090.21+02.32, and IRAS 22198+6336) appeared to present a one-sided lobe, i.e., NGC2264 and G090.21+02.32 showed only a red lobe, and IRAS 22198+6336 presented only a blue lobe.

³ <https://irsa.ipac.caltech.edu/Missions/wise.html>

⁴ <https://irsa.ipac.caltech.edu/Missions/iras.html>

3. We detected HCO^+ molecular outflows for all sources. Eight sources (L1287, G176.51+00.20, Mon R2, NGC2264, G105.41+09.87, IRAS 22198+6336, L1206, and Cep A) showed clear bipolar or multiple outflow structures. G090.21+02.32 showed only a red lobe. Except for L1287 and Cep A, the HCO^+ outflows of the other sources were mapped for the first time.

4. We detected CS molecular outflows for the first time for all sources. Except for G090.21+02.32, which showed only a red lobe, the other eight sources (L1287, G176.51+00.20, Mon R2, NGC2264, G105.41+09.87, IRAS 22198+6336, L1206, and Cep A) presented clear bipolar or multiple outflow structures.

3.2.1. L1287

The ^{12}CO bipolar outflows of L1287 were first detected by Snell et al. (1990), and confirmed by Yang et al. (1991); Xu et al. (2006b). Benefitting from our high-sensitivity observations (see Table 3), the velocity range of the blue lobe of this source has been extended from -31 km s^{-1} (Yang et al. 1991) to -34 km s^{-1} . The -2 km s^{-1} component in the red line wing was contaminated, so the velocity range cannot be extended. After updating the velocity range, the structure of the bipolar outflow remained unchanged. It is aligned along the northeast–southwest direction (see panel (a1) of Figure 3), which is similar to the results of Snell et al. (1990); Yang et al. (1991); Xu et al. (2006b).

L1287’s HCO^+ outflow was mapped by Yang et al. (1991). The velocity ranges have been extended with our data from -23.8 km s^{-1} to -33.0 km s^{-1} for the blue lobe, and from -13.2 km s^{-1} to -6.0 km s^{-1} for the red lobe. Our results are similar to those of Yang et al. (1991).

The ^{13}CO and CS outflows of L1287 were also detected (see panels (c1) and (d1) of Figure 3, respectively), which are also aligned along the northeast–southwest direction. However, the distances between the emission peaks of the red and blue lobes of the ^{13}CO , HCO^+ and CS outflows are smaller than those of ^{12}CO . Compared with the ^{12}CO outflow, the locations of the other three outflows are shifted a little to the southeast direction, so that the midpoint of the red and blue lobes is closer to the position of the IRAS source. Meanwhile, both the ^{12}CO and HCO^+ outflows have larger blue lobes than red ones, while the sizes of the two lobes for ^{13}CO and CS are similar.

IRAS 00338+6312 (see the star in Figure 3) is located at the center of these bipolar outflows. There is also WISE emission located at the center of the four groups of bipolar outflows. The core traced by CS, HCN, HCO^+ , and NH_3 (Walker & Masheder 1997; Zinchenko et al. 1997) are all associated with the IRAS source. Meanwhile, the emission peak of C^{18}O is associated with the IRAS source. All of these tracers seem to indicate that the same source drives all the bipolar outflows.

3.2.2. G176.51+00.20

The velocity range has been extended from -30 km s^{-1} to -47 km s^{-1} in the blue wing and from -5 km s^{-1} to -1 km s^{-1} in the red wing of the ^{12}CO outflow from G176.51+00.20 (which is also named AFGL 5157, and NGC 1985, Snell et al. 1988, see panel (a1) of Figure 4). The ^{12}CO bipolar outflows are along the east–west direction, which is coincident with the results of the study of Snell et al. (1988).

The bipolar outflows of HCO^+ , ^{13}CO , and CS have been mapped for the first time in this work (see panels (b1), (c1), and (d1) of Figure 4, respectively). The directions of the HCO^+ , ^{13}CO , and CS outflows are similar to those of the ^{12}CO outflows. The distances between the emission peaks of the red and blue lobes of the HCO^+ , ^{13}CO , and CS outflows are also smaller than those of ^{12}CO . Different from the other outflows, however, the red and blue lobes of the CS outflow are very close to each other, and its structure is not as extended as the other outflows. We also found that the velocity range of the red lobe of the HCO^+ outflow is even broader than that of the ^{12}CO outflow (see Table 5 and Figure 4).

There is WISE emission located at the center of bipolar outflows, which could be the source of excitation. Although the emission is faint, it is associated with the emission peak of C^{18}O . The nearest IRAS source, IRAS 05345+3157 (see the star in Figure 4), is located near the emission peak of the blue lobe, and it might be the source of excitation of the outflows.

3.2.3. Mon R2

We detected ^{12}CO , HCO^+ , ^{13}CO , and CS outflows in Mon R2. The ^{12}CO bipolar outflow of Mon R2 has been widely studied by many researchers (Bally & Lada 1983; Meyers-Rice & Lada 1991; Xu et al. 2006b). The velocity range of the red wing of the ^{12}CO outflow has been extended from 22 km s^{-1} (Meyers-Rice & Lada 1991) to 30 km s^{-1} . This source is so complex that observations with different resolutions may result in different structural details of its outflows. With beam size used here (i.e., $\sim 50''$), the pair of bipolar outflow in the north (see Xu et al. 2006b)

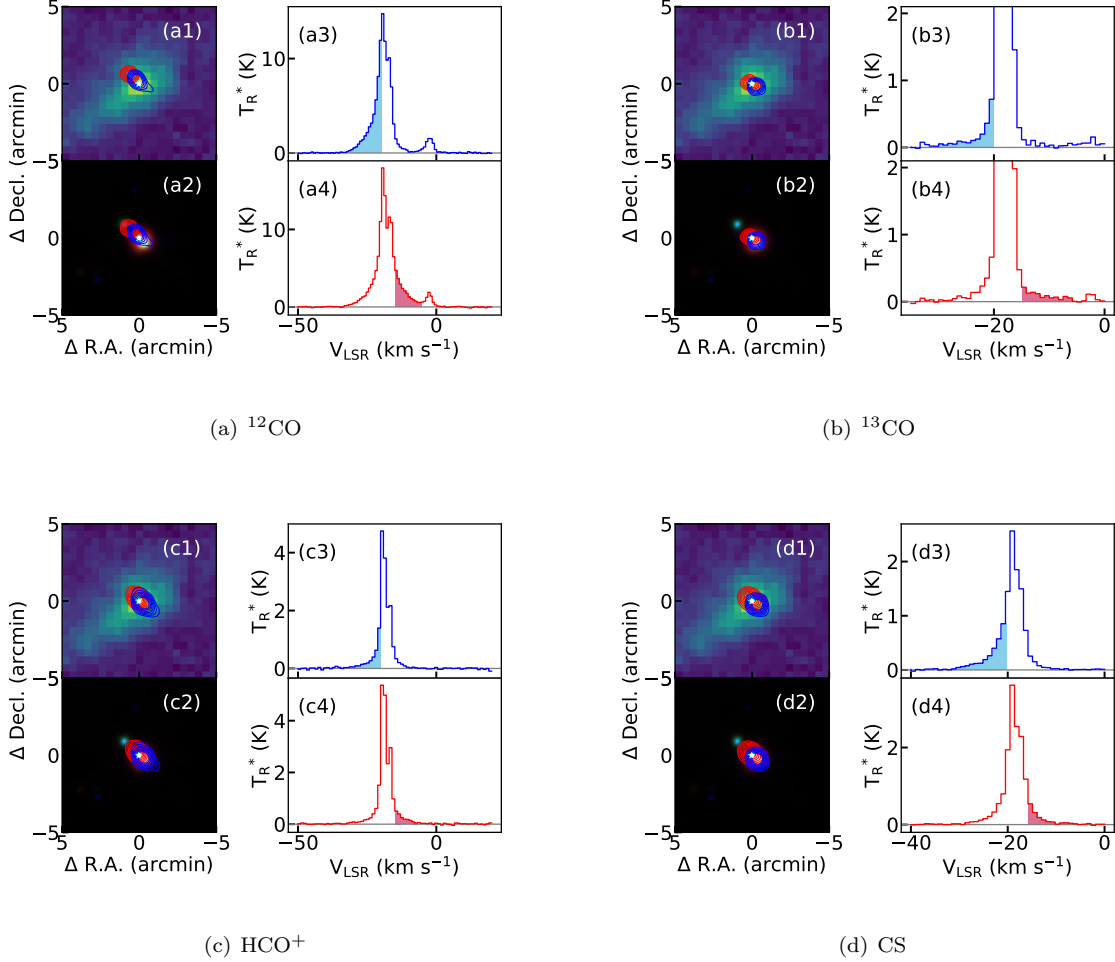


Figure 3. Profile maps of the outflow in L1287. (a1) Integrated C^{18}O map with ^{12}CO blue/red lobe contours (whose levels are from 30% to 90% of the peak intensity of each lobe). The blue star represents the IRAS source (IRAS 00038+6312). The white dot is the emission peak of C^{18}O . Position (0, 0) represents the coordinates of the source (see details in Table 1). (a2) The background shows a false-color RGB WISE image constructed using 4.6 (blue), 12 (green), and 22 μm (red) data, while the other features are the same as in panel (a1). (a3) Blue spectrum of ^{12}CO at the blue emission peak position of the ^{12}CO outflow. The data have been smoothed to $5\delta v$. The blue shading of the spectrum indicates the blue line wing velocity of ^{12}CO . (a4) Red spectrum of ^{12}CO at the red emission peak position of the ^{12}CO outflow. The data have been smoothed to $5\delta v$. The red shading of the spectrum indicates the red line wing velocity of ^{12}CO . For the other subpanels, the descriptions are the same as in panels (a1–a4), but the outflows are of (b1–b4) ^{13}CO , (c1–c4) HCO^+ , and (d1–d4) CS.

partly overlap with the southern bipolar outflow and perhaps also with some surrounding gas. Therefore, the outflow appears relatively extended (see panel (a1) of Figure 5). This morphology is similar to the outflow shown in figure 1 in Meyers-Rice & Lada (1991), where their beam size ($\sim 60''$) was similar to ours. Thus, the structure ascertained in this work is similar to that of Meyers-Rice & Lada (1991), the second pair of bipolar outflows is hard to be separated under current resolution, which might be interfered by other components.

The HCO^+ , ^{13}CO , and CS outflows of this source were mapped for the first time here. Comparing the four groups of outflows, both the ^{12}CO and HCO^+ outflows present two red and blue emission peaks, although these peaks are hard to separate from each other. However, the two peaks in the red lobe of the CS outflow could be easily separated. Furthermore, from the ^{13}CO outflow, only one emission peak can be seen in the red lobe (see Figure 5).

IRAS 06053-0622 is located at the center of the bipolar outflows and near the emission peak of C^{18}O . Meanwhile, the WISE emission of this region is so strong that the WISE data are saturated. All of these tracers seem to indicate that the IRAS source is the source of excitation of these outflows.

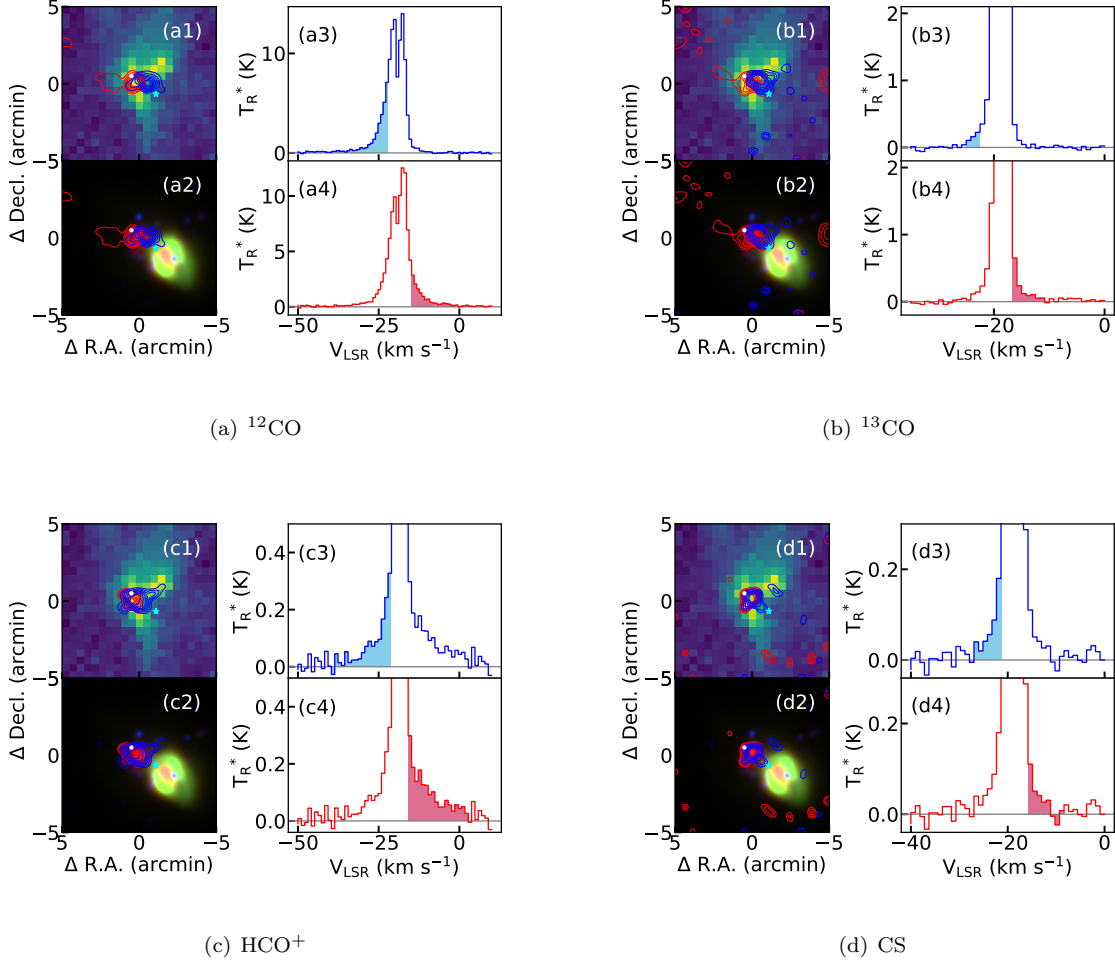


Figure 4. Profile maps of the outflows from G176.51+00.20. The description of each map is the same as that in Figure 3, except the blue star is IRAS 05345+3157.

3.2.4. NGC2264

Previously, only a ^{12}CO red lobe was detected toward NGC2264 (Bally & Lada 1983; Margulis et al. 1988); however, we have also detected a blue lobe (see panel (a1) of Figure 6). Therefore, the ^{12}CO outflow of NGC2264 is not, as once believed, a one-side red lobe, but instead is a bipolar outflow. The emission in the north is so strong (see blue contour in panel (a1) of Figure 6) that it has a disastrous effect on the mapping process of its blue lobe outflow; hence, the blue lobe is easily to be ignored. Thanks to the high-sensitivity observations obtained with PMODLH, we successfully mapped the blue lobe of the outflow.

The ^{13}CO , HCO^+ , and CS outflows of this source were detected for the first time. Except for ^{13}CO , the other outflows of this source are bipolar and distributed along the east–west direction. In fact, the blue line wings of ^{13}CO is higher than the Gaussian fitting, but the structures of the blue lobe in the contour map are too chaotic. Hence, the blue lobe of ^{13}CO , if present, was not detected. The intensities of the blue lobes of HCO^+ and CS are stronger than that of ^{12}CO (see Figure 6).

IRAS 06384+0932 is located at the center of the bipolar outflows. Meanwhile, the WISE emission near the outflow is saturated in this region. Furthermore, the emission peak of C^{18}O is also near the IRAS source and WISE emission. Therefore, IRAS 06384+0932 may be the source of excitation of the outflows.

3.2.5. G090.21+02.32

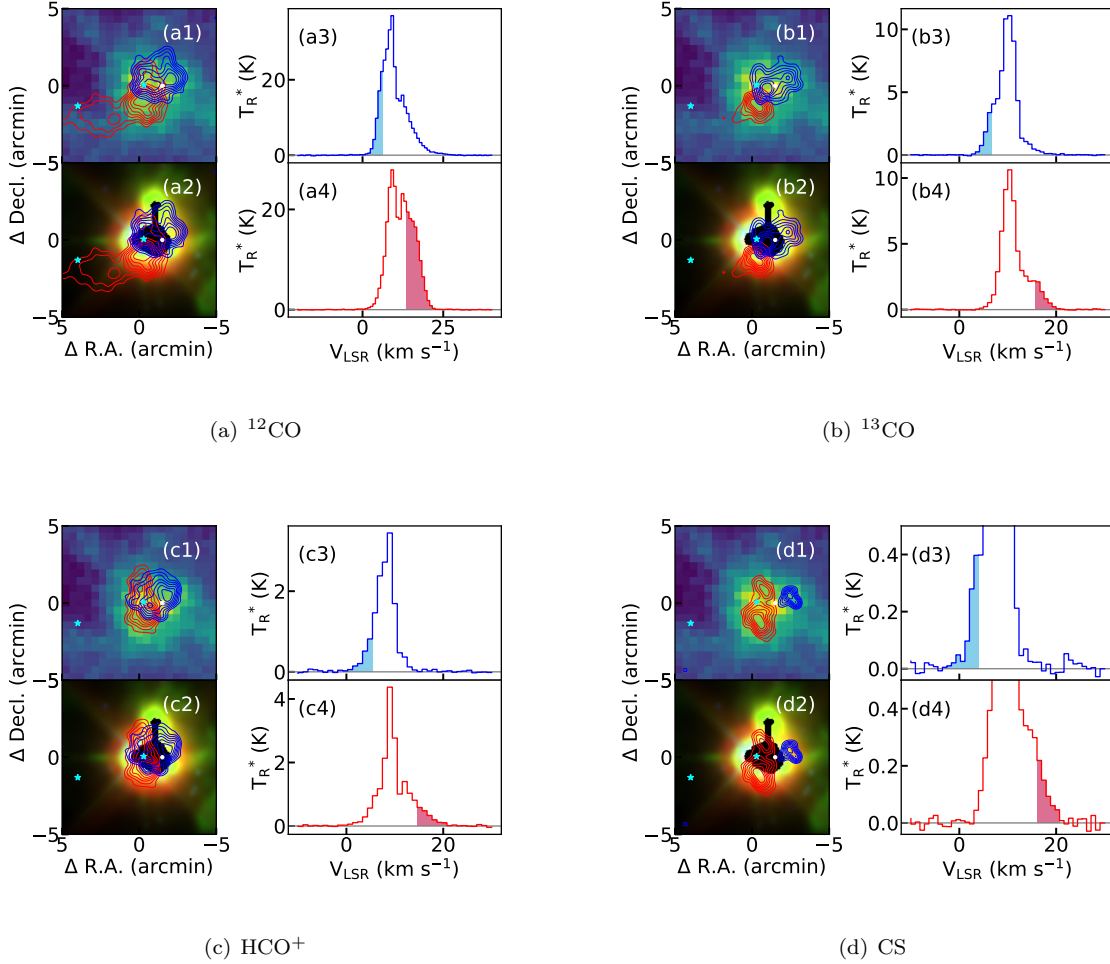


Figure 5. Profile maps of the outflows of Mon R2. The description of each map is the same as that in Figure 3. The blue star at the center is IRAS 06035-0622, and that in the southeast is IRAS 06056-0621.

The ^{12}CO bipolar outflow of G090.21+02.32 was first detected by Clark (1986) (which is near the dark cloud L988a). However, there is strong emission in the blue wing at the peak of the blue lobe in Clark (1986) (see panel (a4) of Figure 7), but this emission cannot be the blue lobe of the ^{12}CO outflow. Instead, we suggest that G090.21+02.32 only possesses a red lobe rather than a bipolar ^{12}CO outflows.

We also detected ^{13}CO , HCO^+ , and CS outflows for the first time for this source. There are multi-velocity components at $\sim 1.0 \text{ km s}^{-1}$ in the CS and ^{13}CO line profiles. Therefore, we considered that there might be two features along the line of sight (see panel (e) of Figure 1), and G090.21+02.32 only has red lobes of ^{13}CO , HCO^+ and CS. The emission intensities of HCO^+ and CS of this source, especially the red lobes of the outflows, are weak.

IRAS 21007+4951 is located near the outflow, which is associated with the H_2O maser, UC H_{II} and WISE emission (Xu et al. 2013; Wood & Churchwell 1989). All of these dense tracers indicate that the IRAS source might be a possible excitation source of the outflows.

3.2.6. G105.41+09.87

G105.41+09.87 is near the open cluster NGC 7129 (Trinidad et al. 2004), and this region is extremely complex. It includes two far-infrared sources (i.e., NGC 7129 FIRS1 and NGC 7129 FIRS2, Bechis et al. 1978) and two Herbig-Haro objects (i.e., HH 103 and HH 105 Edwards & Snell 1983). Fuente et al. (2001) detected multiple ^{12}CO outflows in this region. We also detected three ^{12}CO bipolar outflows, where two are located close to the edge of the figure and the other one is located at the center (see panel (a1) of Figure 8). In this work, we have mainly analyzed the outflows at the center.

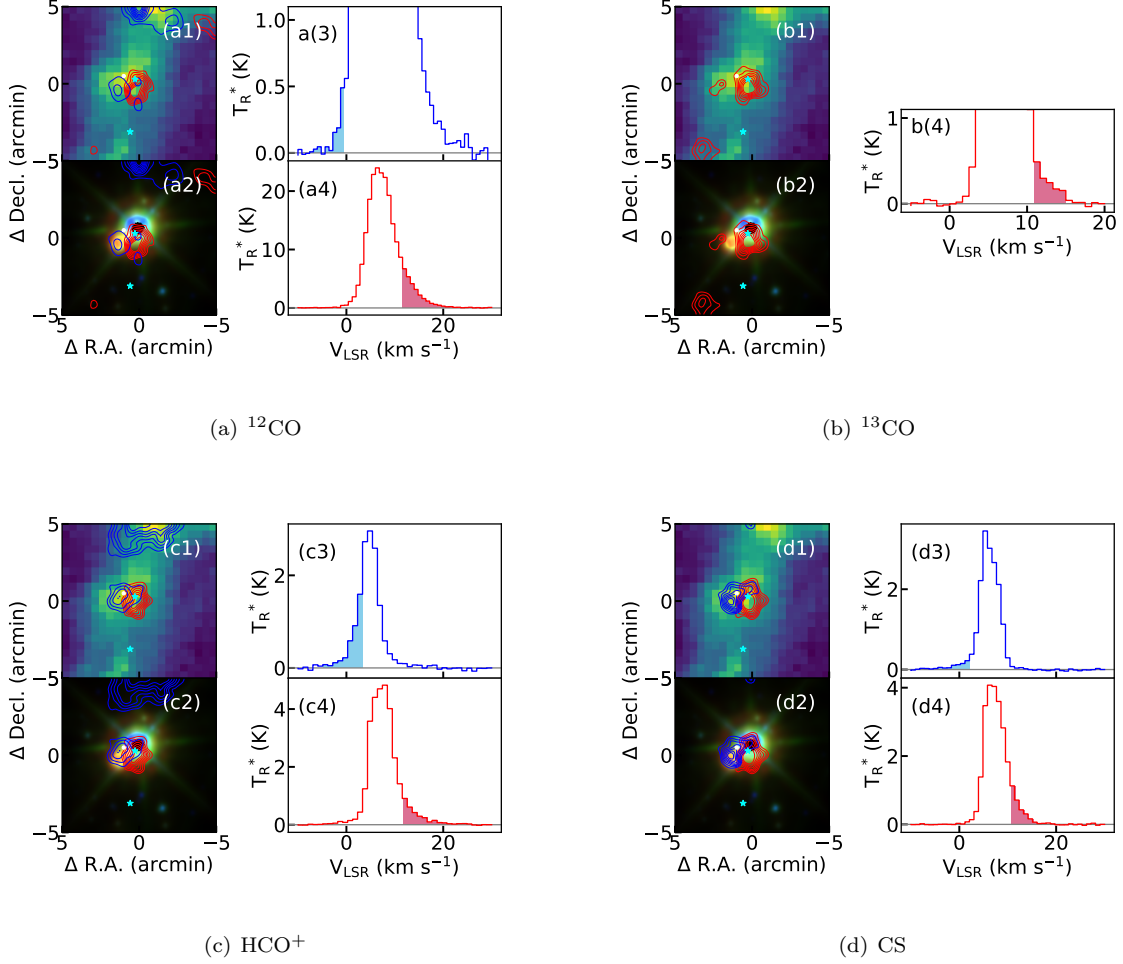


Figure 6. Profile maps of the outflow in NGC2264. The contour levels of the ^{12}CO outflow are from 20% to 90% of the peak intensity of each outflow lobe. The blue star at the center is IRAS 06384+0932, and that at the south is IRAS 06384+0929. The description of each map is the same as that in Figure 3

The ^{13}CO , HCO^+ and CS outflows were detected for the first time. We detect HCO^+ , ^{13}CO and CS bipolar outflows in this region. Similar to the ^{12}CO outflow, we mainly analyzed the bipolar outflow at the center. The ^{12}CO outflow of G105.41+09.87 is extended, while the ^{13}CO , HCO^+ and CS outflows are more concentrated, especially the CS outflows (see Figure 8).

There are two emission peaks of C^{18}O in this region. One is located at the center, which is associated with the IRAS source (IRAS 21418+6552) and the WISE emission, and the other one is located in the south. An H_2O maser is associated with the IRAS source (Xu et al. 2013), so the outflow in the center might be associated with it. Meanwhile, the emission of C^{18}O in the south might be associated with the outflow in the south.

3.2.7. IRAS 22198+6336

IRAS 22198+6336 is located near the dark cloud L1204A. The ^{12}CO bipolar outflows of the source was first studied by Fukui (1989), although detailed description was not provided. Thus, our work is the first to provide a detailed description of the outflows of this source. IRAS 22198+6336 presents not bipolar, but multiple ^{12}CO outflows (see panel (a1) of Figure 9), where the two red lobes are aligned the northwest–southeast direction, and the two blue lobes are aligned the northeast–southwest direction. Meanwhile, these blue and red lobes intersect. As both the red and blue lobes have two peaks, we infer that there are probably two pairs of bipolar outflows in this region. The southern one is along the northeast–southwest direction, and the northern one is along the east–west direction.

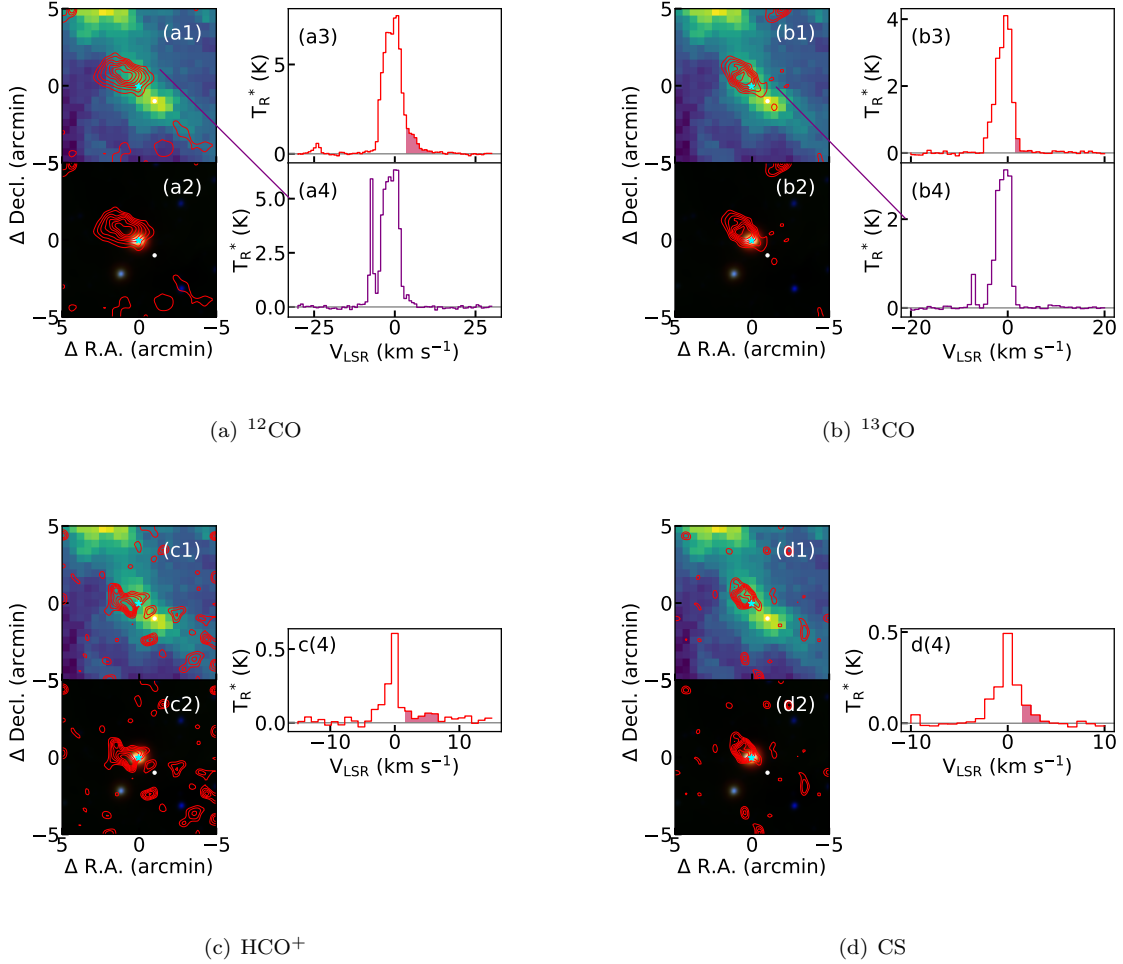


Figure 7. Profile maps of the outflows in G090.21+02.32. Panel (a4) shows the ^{12}CO spectrum at the position which is marked by the endpoint of the straight purple line in (a1), and the position is the peak position of the blue emission found by Clark (1986). Panels (b1–b4) are similar to panels (a1–a4), while the spectrum is from ^{13}CO . The description of each map is the same as that in Figure 3.

We also detected HCO^+ and CS bipolar outflows in this region, as well as the blue lobe of an ^{13}CO outflow. However, different to the structures seen in the ^{12}CO outflows, both the HCO^+ and CS outflows seem to have one pair of bipolar outflow. The blue lobes of the HCO^+ and CS outflows are more concentrated than that of the ^{12}CO outflows. Although the red lobes of the HCO^+ and CS outflows are extended and their structures are different from those of the ^{12}CO outflows, they only have one emission peak. As the brightness temperatures of HCO^+ and CS are relatively lower than those of the other sources, the outflow maps of HCO^+ and CS are weak.

IRAS 22198+6336 is located at the center of the bipolar outflows, and the WISE emission is also near the IRAS source. Hence, IRAS 22198+6336 might be the excitation source of the outflows.

3.2.8. L1206

Only the blue lobe of the ^{12}CO outflow was detected in L1206 by Sugitani et al. (1989); Xu et al. (2006b), while Beltrán et al. (2006) and Liu et al. (2020) successfully detected the blue and red lobes of the ^{12}CO outflow. We also detected a pair of bipolar outflow of this source. Hence, there is a pair of bipolar ^{12}CO outflows in L1206 (see details in panel (a1) of Figure 10). Apart from ^{12}CO , we detected bipolar ^{13}CO , HCO^+ , and CS outflows from this source. The structures of these four groups of outflows are similar, i.e., the extended red lobes are located to the northwest and the compact blue lobes are located at the center. In general, the bipolar outflows are aligned along the northwest–southeast direction. Except for the CS outflow, the red lobes of the ^{12}CO , ^{13}CO , and HCO^+ outflows are

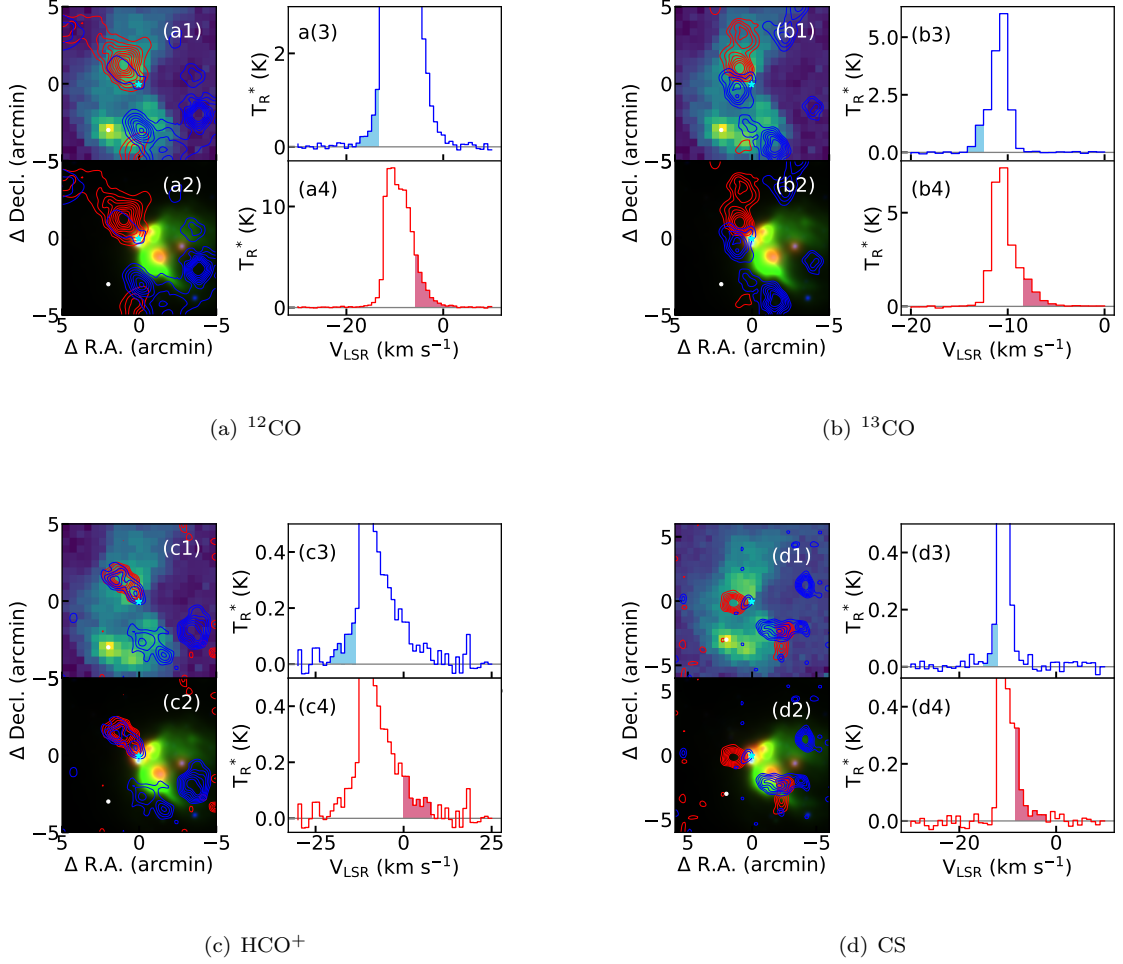


Figure 8. Profile maps of the outflows in G105.41+09.87. The blue star at the center is IRAS 21418+6552, and the contour levels of the ^{12}CO outflow are from 10% to 90% of the peak intensity of each outflow lobe. The other descriptions of each map are the same as those in Figure 3.

complex, where the different components seen in the red lobes are difficult to be separated with each other under the present resolution.

There are two IRAS sources in this region (i.e., IRAS 22272+6358A and IRAS 22272+6358B). IRAS 22272+6358A is located near the center of the bipolar outflows. Meanwhile, there is WISE emission with red color, which implies an earlier object relative to the eastern yellow-green one. The emission peak of C^{18}O is also near IRAS 22272+6358A and the red WISE emission. Therefore, IRAS 22272+6358A might be the source of excitation of the outflows.

3.2.9. *Cep A*

We have detected ^{12}CO , ^{13}CO , HCO^+ , and CS outflows from this source (see Figure 11). The configurations of the ^{12}CO bipolar outflow (see panel (a1) Figure 11) is similar to the results of Rodriguez et al. (1980); Ho et al. (1982); Narayanan & Walker (1996); Xu et al. (2006b). The velocity ranges of the ^{12}CO outflows have been extended from -36 km s^{-1} to -42 km s^{-1} in the blue lobe, and from 14 km s^{-1} to 33 km s^{-1} in the red lobe (Rodriguez et al. 1980). After updating the velocity ranges, the structures of the outflows are also similar to the morphologies detected by Ho et al. (1982); Xu et al. (2006b).

The red lobes of the ^{12}CO , ^{13}CO , and HCO^+ outflows appear to have two peaks. For the CS outflow, there are even three components in the red lobe. The sizes of the blue lobes are similar for the four groups of outflows, but they differ greatly from those of the corresponding red lobes. The red lobes of the ^{13}CO and CS outflows are significantly

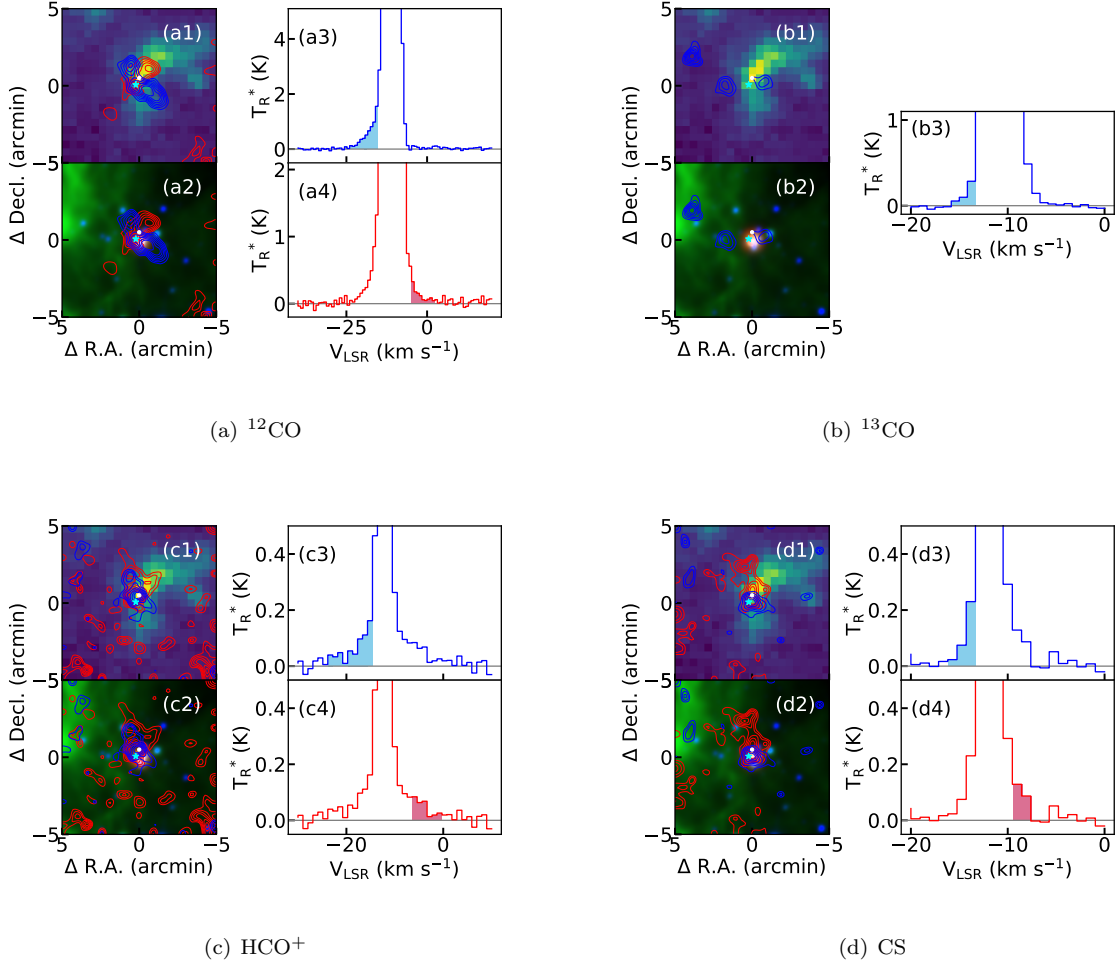


Figure 9. Profile maps of the outflows in IRAS 22198+6336. The description of each map is the same as that in Figure 3. The blue star is IRAS 22198+6336, and the contour levels of the CS outflow are from 40% to 90% of the peak intensity of each outflow lobe.

more extended than those of ^{12}CO and HCO^+ . Different to the other outflows, the ^{13}CO outflow has an additional red lobe in the east.

There are three IRAS sources (IRAS 22543+6145, IRAS 22540+6146, and IRAS 22544+6141) in this region. IRAS 22543+6143, near the white region with strong WISE emission, is located at the center of the bipolar outflows (see Figure 11), which indicates that IRAS 22543+6143 is a possible excitation source of the outflows.

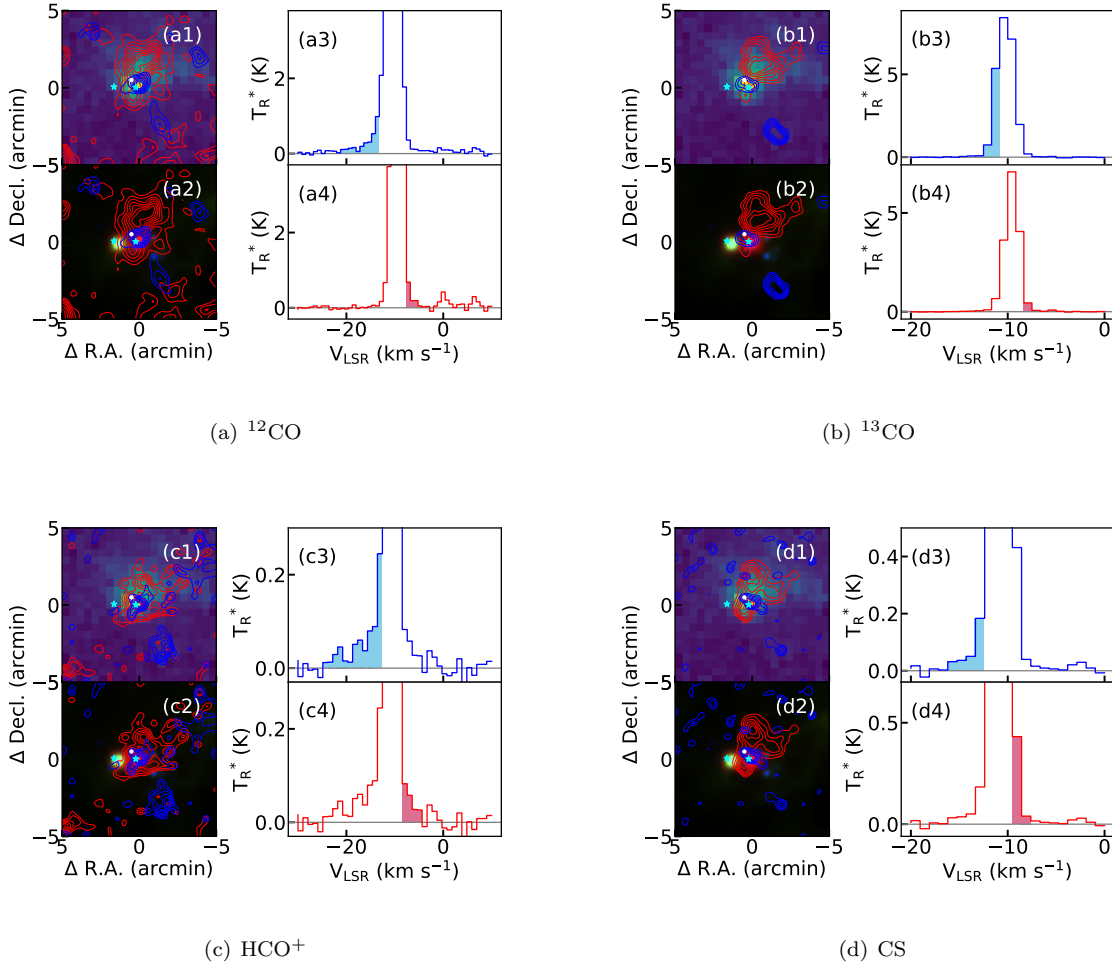


Figure 10. Profile maps of the outflows in L1206. The description of each map is the same as that in Figure 3. The blue star at the center is IRAS 22272+6358A, and that in the east is IRAS 22272+6358B.

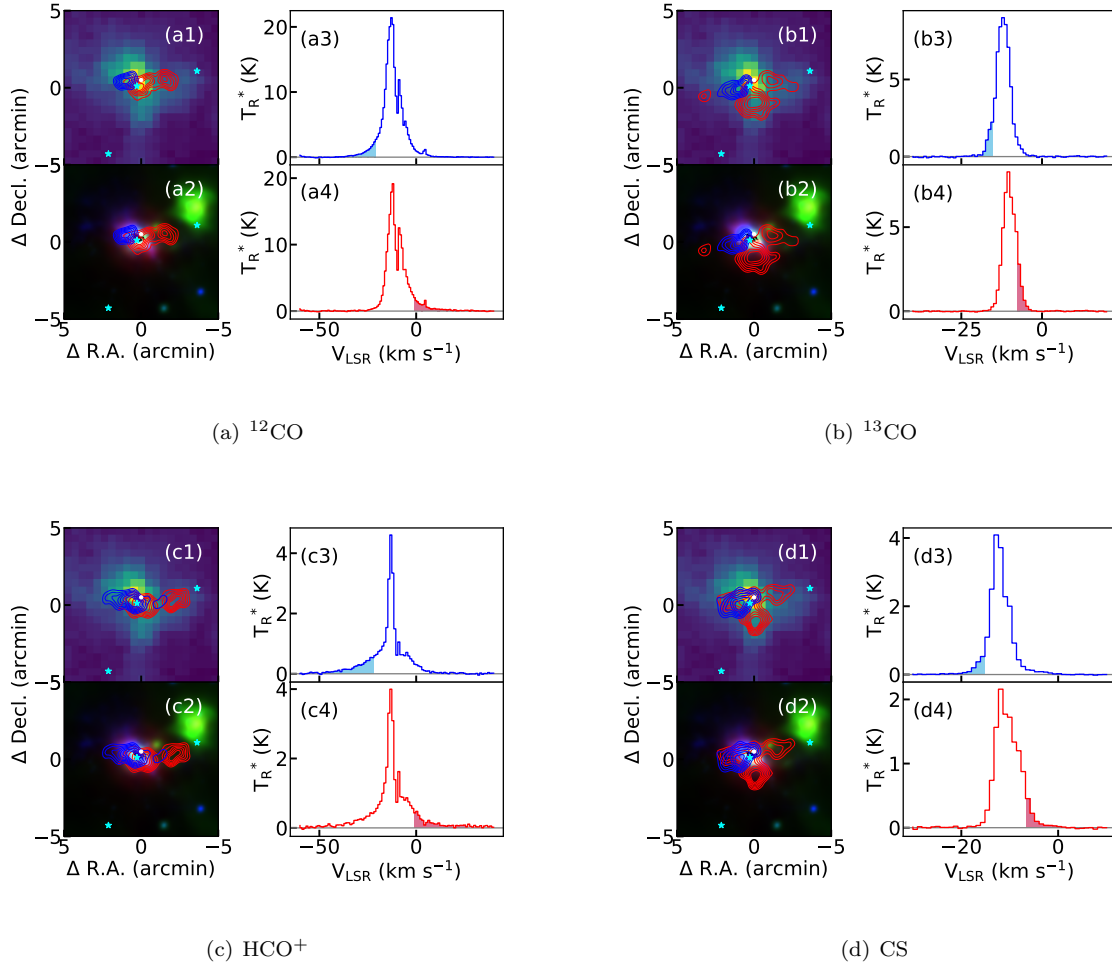


Figure 11. Profile maps of the outflows in Cep A. The description of each map is the same as that in Figure 3. The blue star at the center is IRAS 22543+6145, while that in the southeast is IRAS 22544+6141, and that in the northwest is IRAS 22540+6146.

Table 6. Physical properties of the ^{12}CO outflows.

Source	Index	Lobe	N (10^{20} cm^{-2})	M_{lobe} (M_{\odot})	$\langle \Delta v_{\text{lobe}} \rangle$ (km s^{-1})	l_{lobe} (pc)	P_{lobe} ($M_{\odot} \text{ km s}^{-1}$)	E_{lobe} (10^{44} erg)	t_{lobe} (10^4 yr)	$L_{\text{m(lobe)}}$ ($10^{-2} L_{\odot}$)
(1)	(2)	(3)	(4)	(5)	(6)	(7)	(8)	(9)	(10)	(11)
L1287	1	blue	4.1	2.0	7.7	0.7	15.2	15.9	2.3	53.9
	2	red	3.4	1.1	12.4	0.5	13.6	18.3	1.7	81.7
G176.51+00.20	3	blue	3.1	1.3	15.9	0.6	20.9	42.4	1.0	331.9
	4	red	2.1	0.7	11.3	0.5	8.0	13.4	0.9	119.0
Mon R2	5	blue	3.9	7.3	8.6	1.2	63.3	54.7	5.2	82.0
	6	red	13.4	17.2	12.2	1.0	209.2	257.0	2.3	848.4
NGC2264	7	blue	0.3	0.1	18.2	0.5	1.2	2.1	1.9	8.3
	8	red	3.5	1.4	13.9	0.6	19.6	27.6	1.9	110.5
G090.21+02.32	9	red	0.8	0.5	10.7	0.7	5.9	6.6	3.1	16.3
G105.41+09.87	10	blue	0.4	0.4	9.9	1.0	3.8	5.1	2.4	16.7
	11	red	2.5	2.2	11.4	0.7	24.6	28.6	2.7	82.0
IRAS 22198+6336	12	blue	0.6	0.4	11.4	0.8	4.1	4.9	3.0	12.6
	13
	14	red	0.2	0.1	15.3	0.7	1.0	1.5	2.7	4.2
	15	blue	0.3	0.1	11.4	0.5	0.8	0.9	2.0	3.6
L1206	16	red	0.1	0.1	6.1	0.7	0.5	0.3	6.6	0.4
	17	blue	2.4	0.5	27.7	0.5	15.1	43.3	0.8	431.6
CepA	18	red	2.3	1.2	31.5	0.7	38.9	129.1	0.8	1264.2
	19
Statistic	min		0.1	0.1	6.1	0.5	0.5	0.3	0.8	0.4
	max		13.4	17.2	31.5	1.2	209.2	257.0	6.6	1264.2
	mean		2.5	2.2	13.9	0.7	26.2	38.3	2.4	204.0
	median		2.3	0.7	11.4	0.7	13.6	15.9	2.3	81.7

Table 6 continued on next page

Table 6 (*continued*)

Source	Index	Lobe	N (10^{20} cm^{-2})	M_{lobe} (M_{\odot})	$\langle \Delta v_{\text{lobe}} \rangle$ (km s^{-1})	h_{lobe} (pc)	P_{lobe} ($M_{\odot} \text{ km s}^{-1}$)	E_{lobe} (10^{44} erg)	t_{lobe} (10^4 yr)	$L_{\text{m(lobe)}}$ ($10^{-2} L_{\odot}$)
(1)	(2)	(3)	(4)	(5)	(6)	(7)	(8)	(9)	(10)	(11)

NOTE— (1) Source name. (2) Index. The index of the outflow lobe of each source is unique, and a vacant index corresponds to an outflow of other molecules. (3) Red/blue lobe. (4) H_2 density of the red/blue lobe. (5) Mass of the red/blue lobe. (6) Velocity of the red/blue lobe. (7) Length of the red/blue lobe. (8) Momentum of the red/blue lobe. (9) Kinetic energy of the red/blue lobe. (10) Dynamical timescale of the red/blue lobe. (11) Mechanical luminosity of the red/blue lobe. The last four lines are the mean, median, min, and max values of these parameters.

Table 7. Physical properties of the ^{13}CO outflows.

Source	Index	lobe	N (10^{20} cm^{-2})	M_{lobe} (M_{\odot})	$\langle \Delta v_{\text{lobe}} \rangle$ (km s^{-1})	l_{lobe} (pc)	P_{lobe} ($M_{\odot} \text{ km s}^{-1}$)	E_{lobe} (10^{45} erg)	t_{lobe} (10^4 yr)	$L_{\text{m(lobe)}}$ ($10^{-1} L_{\odot}$)
(1)	(2)	(3)	(4)	(5)	(6)	(7)	(8)	(9)	(10)	(11)
L1287	1	blue	9.9	3.2	9.7	0.5	30.7	3.5	1.9	14.4
	2	red	9.4	3.8	9.7	0.5	36.5	4.2	2.1	15.8
G176.51+00.20	3	blue	3.3	2.3	9.6	0.7	21.8	2.0	5.0	3.1
	4	red	9.8	3.4	5.7	0.5	19.4	1.2	3.4	2.8
Mon R2	5	blue	39.7	48.5	7.8	1.1	376.4	28.2	8.4	26.0
	6	red	42.2	17.2	12.0	0.5	206.4	23.9	2.3	79.2
NGC2264	7
	8	red	12.0	4.8	7.2	0.6	34.7	2.6	4.5	4.4
G090.21+02.32	9	red	6.4	2.4	3.7	0.6	8.9	0.3	6.8	0.4
	10	blue	6.5	6.1	3.7	0.8	22.8	0.8	11.2	0.6
G105.41+09.87	11	red	23.9	17.3	5.5	0.7	95.6	5.3	7.1	5.8
	12	blue1	4.1	2.1	5.1	0.6	10.4	0.5	5.9	0.7
IRAS 22198+6336	13	blue2	4.9	2.7	4.6	0.6	12.6	0.6	5.9	0.7
	14
L1206	15	blue	8.8	2.9	3.5	0.6	10.1	0.3	8.4	0.3
	16	red	8.7	3.8	3.3	0.7	12.6	0.4	8.2	0.4
CepA	17	blue	28.1	8.9	9.9	0.6	87.8	8.5	2.9	22.8
	18	red1	44.4	32.1	7.5	0.7	239.9	17.7	5.1	27.0
Statistic	19	red2	31.7	15.7	7.7	0.6	121.7	9.2	4.1	17.3
	min		3.3	2.1	3.3	0.5	8.9	0.3	1.9	0.3
	max		44.4	48.5	12.0	1.1	376.4	28.2	11.2	79.2
	mean		17.3	10.4	6.8	0.6	79.3	6.4	5.5	13.0
	median		9.8	3.8	7.2	0.6	30.7	2.6	5.1	4.4

NOTE—The description of each column is the same as that of Table 6.

Table 8. Physical properties of the HCO⁺ outflows.

Source	Index	lobe	N (10^{21} cm^{-2})	M_{lobe} (M_{\odot})	$\langle \Delta v_{\text{lobe}} \rangle$ (km s^{-1})	l_{lobe} (pc)	P_{lobe} ($10 M_{\odot} \text{ km s}^{-1}$)	E_{lobe} (10^{45} erg)	t_{lobe} (10^4 yr)	$L_{\text{m(lobe)}}$ (L_{\odot})
(1)	(2)	(3)	(4)	(5)	(6)	(7)	(8)	(9)	(10)	(11)
L1287	1	blue	3.0	14.4	8.5	0.5	122.8	14.0	1.6	6.7
	2	red	2.8	11.0	11.1	0.5	122.7	14.7	1.9	5.9
G176.51+00.20	3	blue	1.4	11.8	16.1	0.8	189.1	38.7	2.0	15.2
	4	red	2.4	4.1	14.3	0.5	58.8	11.3	1.1	7.8
Mon R2	5	blue	1.9	29.8	9.6	1.0	287.1	27.6	4.7	4.5
	6	red	2.5	28.3	14.2	1.0	400.7	56.4	3.9	11.2
NGC2264	7	blue	2.3	17.5	7.3	0.7	128.1	11.0	3.5	2.4
	8	red	4.0	16.1	13.2	0.6	213.0	29.1	2.2	10.4
G090.21+02.32	9	red	0.3	1.1	6.7	0.6	7.2	0.5	4.7	0.1
G105.41+09.87	10	blue	0.6	6.4	9.2	1.0	58.4	5.8	4.9	0.9
	11	red	0.9	7.5	26.7	0.8	200.3	51.8	2.1	19.0
IRAS 22198+6336	12	blue	0.7	1.8	9.4	0.6	17.3	1.9	2.6	0.6
	13
L1206	14	red	0.3	1.6	13.6	0.8	22.1	2.9	4.3	0.5
	15	blue	0.6	1.3	5.7	0.5	7.4	0.5	3.3	0.1
CepA	16	red	0.4	2.3	5.0	0.7	11.6	0.6	5.8	0.1
	17	blue	7.5	23.6	32.5	0.6	765.8	272.9	0.8	263.0
Statistic	18	red1	4.1	9.1	34.1	0.6	311.8	114.5	0.8	115.7
	19	red2	4.6	18.7	37.4	0.6	700.6	282.7	0.7	294.9
	min		0.3	1.1	5.0	0.5	7.2	0.5	0.7	0.1
	max		7.5	29.8	37.4	1.0	765.8	282.7	5.8	294.9
	mean		2.2	11.5	15.3	0.7	201.4	52.1	2.8	42.2
	median		2.1	10.1	12.2	0.6	125.4	14.3	2.4	6.3

NOTE—The description of each column is the same as that of Table 6.

Table 9. Physical properties of the CS outflows.

Source	Index	Lobe	N (10^{20} cm^{-2})	M_{lobe} (M_{\odot})	$\langle \Delta v_{\text{lobe}} \rangle$ (km s^{-1})	l_{lobe} (pc)	$P(\text{lobe})$ ($M_{\odot} \text{ km s}^{-1}$)	$E(\text{lobe})$ (10^{44} erg)	t_{lobe} (10^4 yr)	$L_{\text{m}(\text{lobe})}$ ($10^{-2} L_{\odot}$)
(1)	(2)	(3)	(4)	(5)	(6)	(7)	(8)	(9)	(10)	(11)
L1287	1	blue	12.8	4.1	8.0	0.5	32.4	32.4	1.8	136.3
	2	red	7.1	3.4	9.8	0.5	33.0	35.5	1.9	143.1
G176.51+00.20	3	blue	1.6	0.6	8.2	0.5	4.6	3.8	2.6	11.2
	4	red	1.2	0.6	9.8	0.6	6.1	6.4	2.7	18.2
Mon R2	5	blue	2.8	0.4	14.1	0.5	5.3	7.3	1.9	29.2
	6	red	2.6	2.1	14.7	0.7	31.5	44.3	3.3	103.1
NGC2264	7	blue	3.6	1.1	10.1	0.5	10.9	11.5	2.1	41.6
	8	red	16.8	8.4	9.5	0.7	79.8	76.4	3.7	158.9
G090.21+02.32	9	red	0.8	0.2	4.3	0.5	0.9	0.4	5.1	0.6
G105.41+09.87	10	blue	0.8	0.3	4.8	0.6	1.6	0.8	6.1	1.0
	11	red	2.5	1.1	5.7	0.5	6.1	3.4	5.5	4.7
IRAS 22198+6336	12	blue	0.7	0.3	3.9	0.6	1.1	0.4	11.1	0.3
	13
L1206	14	red	0.7	0.5	4.9	0.7	2.2	1.0	11.4	0.7
	15	blue	1.1	0.2	5.8	0.5	1.4	0.8	3.9	1.6
CepA	16	red	3.9	2.2	2.4	0.6	5.2	1.3	10.1	1.0
	17	blue	5.5	2.7	7.6	0.7	20.7	15.4	5.0	24.1
Statistic	18	red1	4.8	3.2	13.1	0.8	42.0	55.0	3.5	123.0
	19	red2	2.8	1.0	11.9	0.6	12.0	14.4	2.7	41.6
	min		0.7	0.2	2.4	0.5	0.9	0.4	1.8	0.3
	max		16.8	8.4	14.7	0.8	79.8	76.4	11.4	158.9
	mean		3.5	1.7	8.3	0.6	15.5	16.4	4.9	41.4
	median		2.7	1.0	8.1	0.6	6.1	6.8	3.6	21.2

NOTE—The description of each column is the same as that of Table 6.

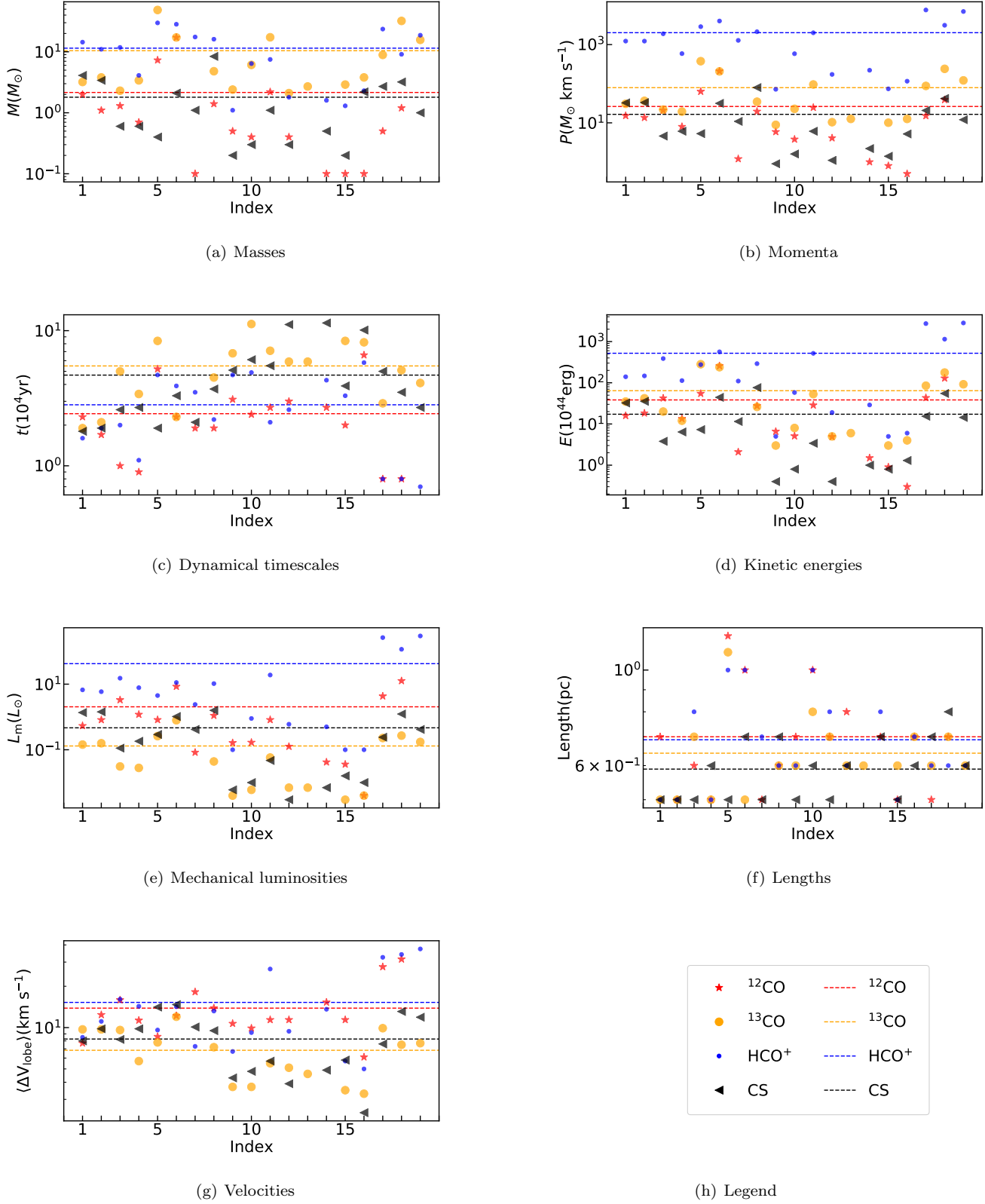


Figure 12. The distributions of the physical properties of the outflows. The dashed lines are the mean value of the physical properties. The meaning of each index is given in Tables 6 – 9.

3.3. Physical properties of the outflows

Due to the accurate distances of these nearby sources and the high-sensitivity observations, we have obtained more accurate physical properties than found previously for these objects. The lengths, masses, momenta, kinetic energies, mechanical luminosities, and dynamical timescales were calculated (see Appendix A). The physical quantities of these molecular lines are summarized in Tables 6 – 9, and the distributions of these quantities are displayed in Figure 12. For ^{12}CO , ^{13}CO , and CS, the molecular outflow of each lobe has a typical momentum of a few $10 M_{\odot} \text{ km s}^{-1}$, a kinetic energy of a few 10^{45} erg, a dynamical timescale of a few 10^4 yr, and a mechanical luminosity of a few $10^{-1} L_{\odot}$. However, the momenta, kinetic energies and mechanical luminosities of the HCO^+ outflows are an order of magnitude larger than those of ^{12}CO , ^{13}CO and CS. The typical outflow mass for ^{13}CO and HCO^+ is a few $10 M_{\odot} \text{ km s}^{-1}$, which is an order magnitude larger than ^{12}CO and CS. Although the masses of ^{13}CO outflow is similar to HCO^+ , the momenta, kinetic energies and mechanical luminosities of ^{13}CO are lower than those of HCO^+ . It might result from the outflow velocity for HCO^+ is much larger than ^{13}CO . However, there is no order of magnitude difference in the dynamical timescales of these four kinds of outflows.

We also obtained more accurate outflow velocities ($\langle \Delta v \rangle$) than previously found, where our results show that $\langle \Delta v \rangle(^{12}\text{CO}) \approx \langle \Delta v \rangle(\text{HCO}^+) > \langle \Delta v \rangle(\text{CS}) \approx \langle \Delta v \rangle(^{13}\text{CO})$. This relationship might indicate that relatively high-velocity outflows can be traced by ^{12}CO and HCO^+ , and relatively low-velocity outflows can be traced by ^{13}CO and CS. In our survey, the typical dynamical timescales (t) of our samples are lower than those found by Beuther et al. (2002); Zhang et al. (2005). Meanwhile, the results show that $t_{^{13}\text{CO}} \approx t_{\text{CS}} > t_{^{12}\text{CO}} \approx t_{\text{HCO}^+}$. Considering that different gases trace different parts of the molecular clouds, the results seem to indicate that the inner gas (traced by ^{13}CO and CS) flows relatively slower than the outer gas (traced by ^{12}CO and HCO^+). Meanwhile, the outer gas might disperse earlier than the inner gas. However, due to the limited number of objects in our sample (i.e., only nine sources), a larger sample size is needed to confirm/refute this tentative conclusion.

3.4. Correlations between the outflow mass, mechanical luminosity and bolometric luminosity of the central sources

A positive correlation was found between the masses (M) of the outflows and the bolometric luminosities (L_{bol}) of the central IRAS sources (see Eq. B9 and Figure 13), where the slope of the best-fitting line is similar to that found by Wu et al. (2004); Maud et al. (2015). This correlation suggests that the mass of an outflow probably depends on the nature of the central source (Bally & Lada 1983; Wu et al. 2004; Maud et al. 2015). Furthermore, the effect of the central star on the surrounding gas seems to increase from the inside out, because the slope of the best-fitting line of the molecules tracing the outer gas is greater than that tracing the inner gas.

Similar to the results of Bontemps et al. (1996); Churchwell (1997); Wu et al. (2004); Maud et al. (2015), we also find that the mechanical force ($F = P/\langle \Delta v \rangle$), the mass rate of the outflow ($\dot{M} = M/t$), and mechanical luminosity (L_m) correlate with the bolometric luminosity of the central IRAS source (see details in Eqs. B10 – B12, and Figures 15 – 16), where the power-law indices of the best-fitting lines among those physical properties are similar to those found by Wu et al. (2004) and Maud et al. (2015). In addition, these relationships also imply that the bolometric luminosity of the central IRAS sources and mechanical luminosity of the outflow are probably correlated with the other physical properties (e.g., the accretion rate). Hence, we suggest the following dependencies: bolometric luminosity \rightarrow accretion rate \rightarrow mass-loss rate in the outflow \rightarrow mechanical luminosity of outflow (see also Wu et al. 2004). Indeed, we find that the mass-loss rates in the outflows are correlated with the mechanical luminosities of the outflows (see Eq. B13 and Figure 17). This dependency was also found by Maud et al. (2015), who had indicated that the central source with higher bolometric luminosity might entrain more material and thus can drive more powerful and more energetic outflow.

4. SUMMARY

We searched for outflows using multi-molecular lines toward nine nearby HMSFRs with accurate distances with the 14-m PMODLH millimeter-wavelength telescope. The main results of our study are summarized as follows:

1. ^{12}CO , ^{13}CO , HCO^+ , and CS outflows were detected toward all nine sources (i.e., the detection rate of all outflows was 100%). Bipolar or multiple outflows of ^{12}CO , HCO^+ , and CS were detected for eight sources (i.e., the detection rate was about 89%). Bipolar outflows of ^{13}CO were detected for six sources (i.e., the detection rate was about 67%).
2. The full line widths of different molecules may have the following relationship: $\Delta V_{^{12}\text{CO}} > \Delta V_{\text{HCO}^+} > \Delta V_{\text{CS}} \approx \Delta V_{^{13}\text{CO}} > \Delta V_{^{18}\text{CO}}$.

3. ^{12}CO and HCO^+ can be used to trace relatively high-velocity outflows, and ^{13}CO and CS can be used to trace relatively low-velocity outflows.

4. The dynamical timescale of different molecules may have the following relationship: $t_{^{13}\text{CO}} \approx t_{\text{CS}} > t_{^{12}\text{CO}} \approx t_{\text{HCO}^+}$.

5. There was a strong correlation between the bolometric luminosity of the central IRAS source and the mechanical luminosities of the outflows (including ^{12}CO , ^{13}CO , HCO^+ and CS), and between the bolometric luminosities and outflow masses. The former correlation suggests a flow dependence, i.e., bolometric luminosity \rightarrow accretion rate \rightarrow mass-loss rate in the outflow \rightarrow mechanical luminosity of outflow. The latter relationship indicates that the mass of the outflow probably depends on its driving source.

ACKNOWLEDGMENTS

We are grateful to all the staff of Purple Mountain Observatory Delingha, especially our observer colleagues for obtaining the excellent observations. We would like to thank the anonymous referee. This work was funded by the NSFC, under grant numbers 11933011, 11873019, and 11673066, and by the Key Laboratory for Radio Astronomy. The research work was also supported by the National Natural Science Fund Committee of the Chinese Academy of Sciences Astronomical Union Funds No. U1731124, U2031202.

APPENDIX

A. DERIVING THE OUTFLOW PARAMETERS

The H_2 column density, $N(\text{H}_2)$, traced by ^{12}CO is given as [Snell et al. \(1984\)](#)

$$N(\text{H}_2) = 4.2 \times 10^{17} \frac{T_{\text{ex}}}{e^{-5.5/T_{\text{ex}}}} \int T_{\text{mb}} dv. \quad (\text{A1})$$

where the velocity range to be integrated is that of the wing range. In this equation we assume that the gas is in local thermodynamic equilibrium (LTE), $X(^{12}\text{CO}) = [^{12}\text{CO}]/[\text{H}_2] = 10^{-4}$ ([Snell et al. 1984](#)), and the excitation temperature, T_{ex} , is 30 K.

The H_2 column density, $N(\text{H}_2)$, traced by ^{13}CO is [Wilson et al. \(2013\)](#)

$$N(\text{H}_2) = 2.3 \times 10^{19} \frac{T_{\text{ex}}}{e^{-5.3/T_{\text{ex}}}} \int T_{\text{mb}} dv \quad (\text{A2})$$

where the velocity range to be integrated is that of the line's wings. In this equation we assume that the gas is in LTE, $X(^{13}\text{CO}) = [^{13}\text{CO}]/[\text{H}_2] = 2 \times 10^{-6}$, and $T_{\text{ex}} = 30$ K ([Li et al. 2016](#)).

The H_2 column density, $N(\text{H}_2)$, traced by HCO^+ can be found as [Yang et al. \(1991\)](#)

$$N(\text{H}_2) = 1.87 \times 10^{19} \frac{T_{\text{ex}}}{1 - e^{-4.3/T_{\text{ex}}}} \int T_{\text{mb}} dv. \quad (\text{A3})$$

where the integration range is over the range of the wings. In this equation we assume that the gas is in LTE, $X(\text{HCO}^+) = [\text{HCO}^+]/[\text{H}_2] = 10^{-8}$ ([Turner et al. 1997](#)) and $T_{\text{ex}} = 15$ K.

The H_2 column density, $N(\text{H}_2)$, traced by CS is

$$N(\text{H}_2) = 3 \times 10^9 \frac{k^2 T_{\text{ex}}}{4\pi^3 \mu_d^2 h v e^{-hv/kT_{\text{ex}}}} \int T_{\text{mb}} dv \quad (\text{A4})$$

where k is the Boltzmann constant (1.38×10^{-16} erg K $^{-1}$), h is the Planck constant (6.626×10^{-27} erg s), μ_d is the dipole moment (1.96 D), and v is the transition frequency (97.981 GHz). The velocity range of integration is that of the wing's range. In this equation we assume that the gas is in LTE, $X(\text{CS}) = [\text{CS}]/[\text{H}_2] = 10^{-9}$, and $T_{\text{ex}} = 20$ K ([Tatematsu et al. 1998](#)).

The mass of the outflow lobe, M_{lobe} , can be found as:

$$M_{\text{lobe}} = N_{\text{lobe}} A_{\text{lobe}} \mu m_{\text{H}} \quad (\text{A5})$$

where A_{lobe} represents the area of the blue/red lobes of outflows, $\mu = 2.72$ is the mean molecular weight, and m_{H} is the hydrogen molecule (Garden et al. 1991). The area was estimated by the region covered by 50% of the outflow peak.

The momentum (P_{lobe}) and kinetic energy (E_{lobe}) of an outflow lobe are, respectively:

$$P_{\text{lobe}} = \sum_{A_{\text{lobe}}} M_{\text{lobe}} \langle \Delta v_{\text{lobe}} \rangle, \quad (\text{A6})$$

and

$$E_{\text{lobe}} = \frac{1}{2} \sum_{A_{\text{lobe}}} M_{\text{lobe}} \langle \Delta v_{\text{lobe}}^2 \rangle. \quad (\text{A7})$$

where $\langle \Delta v_{\text{lobe}} \rangle$ and $\langle \Delta v_{\text{lobe}}^2 \rangle$ are the velocity (i.e., the relative velocity with respect to the central velocity), and the square of the velocity of an outflow lobe (see detail in Li et al. 2018). The mechanical luminosity (L_{lobe}) of an outflow lobe is

$$L_{\text{lobe}} = E_{\text{lobe}}/t_{\text{lobe}} \quad (\text{A8})$$

where $t_{\text{lobe}} = l_{\text{lobe}}/\Delta v_{\text{max}}$, Δv_{max} is the maximum outflow lobe velocity, and l_{lobe} is the length of the outflow.

As it is hard to determine the inclination angle of an outflow, we have adopted a mean inclination angle of 57.3° to conform with similar studies (Bontemps et al. 1996). The inclination and blending correction factors are cited (Li et al. 2019, see table 5 of that paper).

B. RELATIONSHIP BETWEEN THE OUTFLOW MASS, MECHANICAL LUMINOSITY AND BOLOMETRIC LUMINOSITY OF THE CENTRAL SOURCES

The mass, M , of the ^{12}CO , ^{13}CO , HCO^+ , and CS outflows as a function of the bolometric luminosity, L_{bol} , of the central IRAS source is as follows (see Figure 13):

$$\log M(^{12}\text{CO}) = (0.46 \pm 0.17) \log L_{\text{bol}} + (-2.63 \pm 0.57), r = 0.57; \quad (\text{B9a})$$

$$\log M(^{13}\text{CO}) = (0.44 \pm 0.07) \log L_{\text{bol}} + (-0.65 \pm 0.24), r = 0.85; \quad (\text{B9b})$$

$$\log M(\text{HCO}^+) = (0.49 \pm 0.09) \log L_{\text{bol}} + (-0.74 \pm 0.29), r = 0.82; \quad (\text{B9c})$$

$$\log M(\text{CS}) = (0.24 \pm 0.14) \log L_{\text{bol}} + (-0.79 \pm 0.47), r = 0.40. \quad (\text{B9d})$$

The mass outflow rate, \dot{M} , of the ^{12}CO , ^{13}CO , HCO^+ , and CS outflows as a function of the bolometric luminosity, L_{bol} , of the central IRAS source is as follows (see Figure 14):

$$\log \dot{M}(^{12}\text{CO}) = (0.54 \pm 0.19) \log L_{\text{bol}} + (-6.19 \pm 0.62), r = 0.60; \quad (\text{B10a})$$

$$\log \dot{M}(^{13}\text{CO}) = (0.51 \pm 0.07) \log L_{\text{bol}} + (-5.55 \pm 0.24), r = 0.87; \quad (\text{B10b})$$

$$\log \dot{M}(\text{HCO}^+) = (0.63 \pm 0.13) \log L_{\text{bol}} + (-5.56 \pm 0.43), r = 0.78; \quad (\text{B10c})$$

$$\log \dot{M}(\text{CS}) = (0.37 \pm 0.17) \log L_{\text{bol}} + (-5.79 \pm 0.56), r = 0.48. \quad (\text{B10d})$$

The outflow force, F , of the ^{12}CO , ^{13}CO , HCO^+ , and CS outflows as a function of the bolometric luminosity, L_{bol} , of the central IRAS source is as follows (see Figure 15):

$$\log F(^{12}\text{CO}) = (0.64 \pm 0.21) \log L_{\text{bol}} + (-5.45 \pm 0.70), r = 0.61; \quad (\text{B11a})$$

$$\log F(^{13}\text{CO}) = (0.65 \pm 0.10) \log L_{\text{bol}} + (-5.20 \pm 0.34), r = 0.86; \quad (\text{B11b})$$

$$\log F(\text{HCO}^+) = (0.82 \pm 0.17) \log L_{\text{bol}} + (-4.08 \pm 0.58), r = 0.76; \quad (\text{B11c})$$

$$\log F(\text{CS}) = (0.56 \pm 0.19) \log L_{\text{bol}} + (-5.55 \pm 0.65), r = 0.59. \quad (\text{B11d})$$

The mechanical luminosity, L_{m} , of the ^{12}CO , ^{13}CO , HCO^+ , and CS outflows as a function of the bolometric luminosity, L_{bol} , of the central IRAS source is as follows (see Figure 16):

$$\log L_m(^{12}\text{CO}) = (0.71 \pm 0.24) \log L_{\text{bol}} + (-1.64 \pm 0.79), r = 0.61; \quad (\text{B12a})$$

$$\log L_m(^{13}\text{CO}) = (0.77 \pm 0.14) \log L_{\text{bol}} + (-2.90 \pm 0.48), r = 0.81; \quad (\text{B12b})$$

$$\log L_m(\text{HCO}^+) = (0.98 \pm 0.23) \log L_{\text{bol}} + (-2.56 \pm 0.78), r = 0.73; \quad (\text{B12c})$$

$$\log L_m(\text{CS}) = (0.75 \pm 0.23) \log L_{\text{bol}} + (-3.39 \pm 0.77), r = 0.63. \quad (\text{B12d})$$

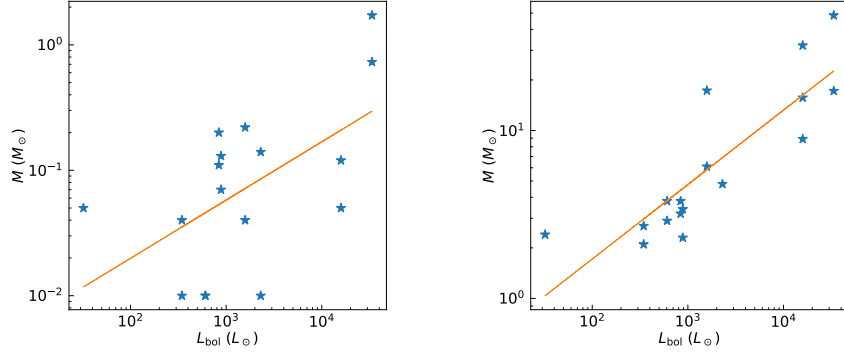
The mass outflow rate, \dot{M} , of the ^{12}CO , ^{13}CO , HCO^+ , and CS outflows as a function of the mechanical luminosity, L_m , of the outflows is as follows (see Figure 17):

$$\log \dot{M}(^{12}\text{CO}) = (0.72 \pm 0.07) \log L_m + (-4.20 \pm 0.07), r = 0.93; \quad (\text{B13a})$$

$$\log \dot{M}(^{13}\text{CO}) = (0.58 \pm 0.05) \log L_m + (-3.09 \pm 0.08), r = 0.94; \quad (\text{B13b})$$

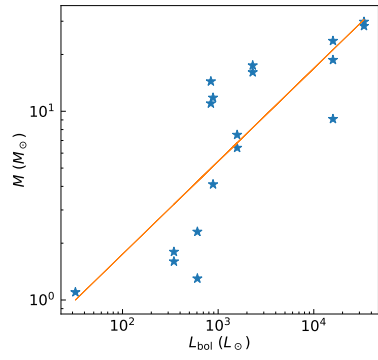
$$\log \dot{M}(\text{HCO}^+) = (0.57 \pm 0.05) \log L_m + (-3.87 \pm 0.06), r = 0.94; \quad (\text{B13c})$$

$$\log \dot{M}(\text{CS}) = (0.61 \pm 0.06) \log L_m + (-4.01 \pm 0.08), r = 0.94. \quad (\text{B13d})$$

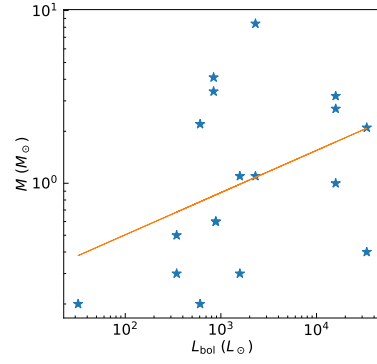


(a) ^{12}CO

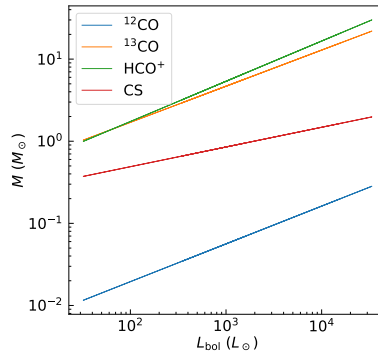
(b) ^{13}CO



(c) HCO^+



(d) CS



(e) Fitting lines

Figure 13. The mass (M) of different molecular outflows as a function of the bolometric luminosity (L_{bol}) of the central IRAS source. Each molecular line is given at the bottom of each panel. Panel (e) is the least-square fitting lines of the four molecular outflows.

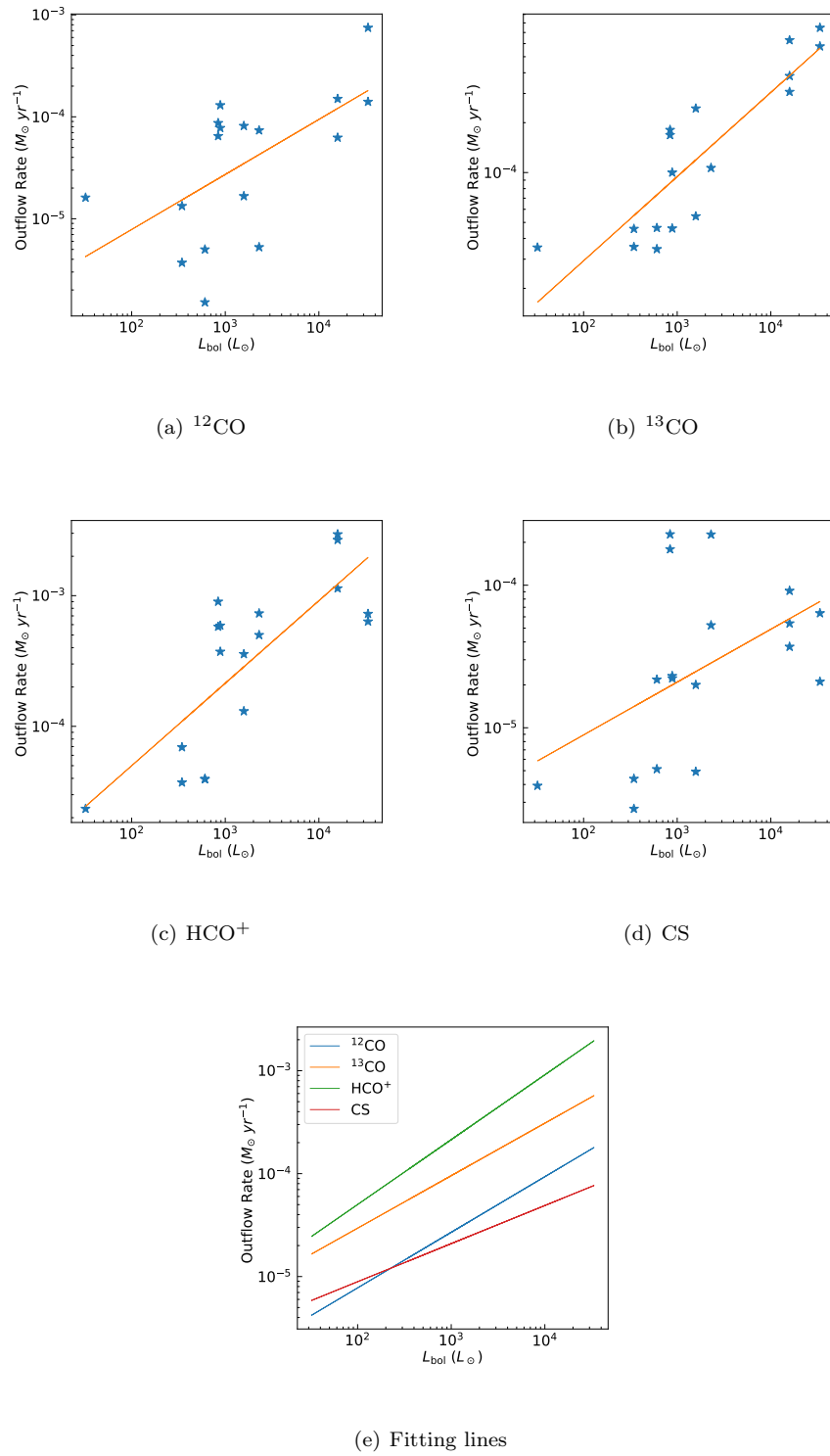
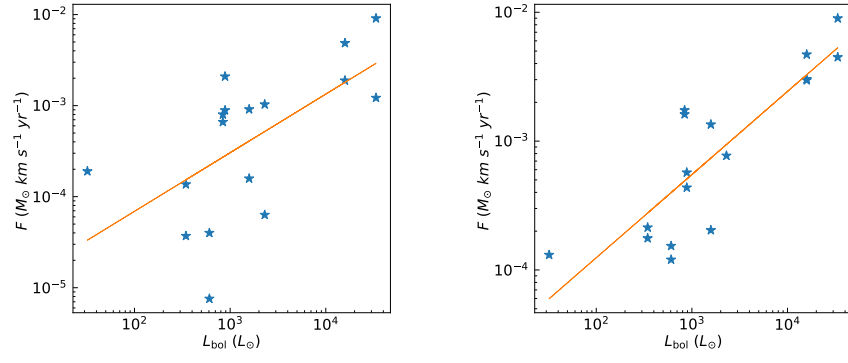
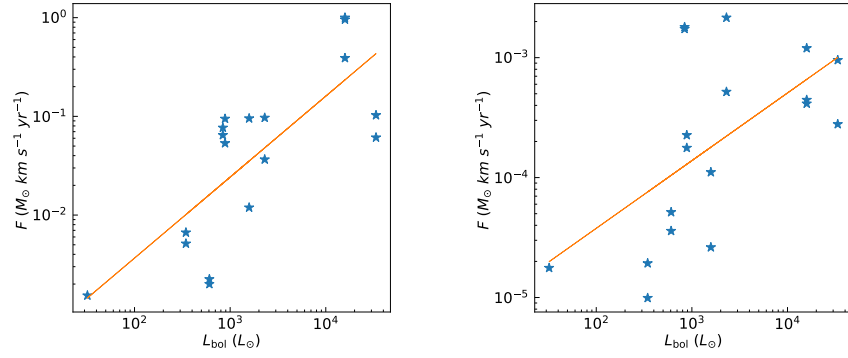


Figure 14. The mass outflow rate (\dot{M}) of different molecular outflows as a function of the bolometric luminosity (L_{bol}) of the central IRAS source. Each molecular line is indicated at the bottom of each panel. Panel (e) is the least-square fitting lines of the four molecular outflows.



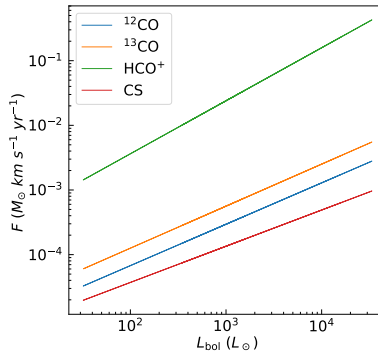
(a) ^{12}CO

(b) ^{13}CO



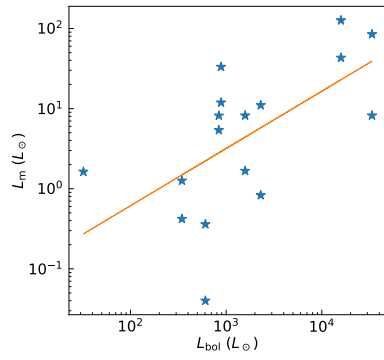
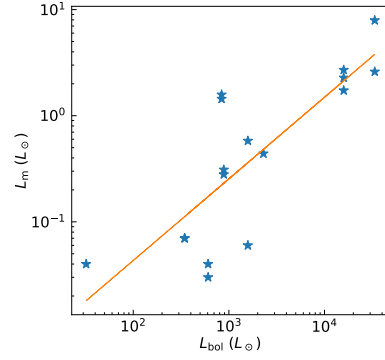
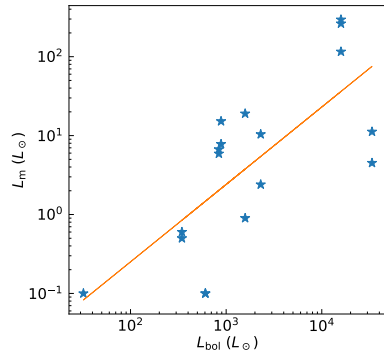
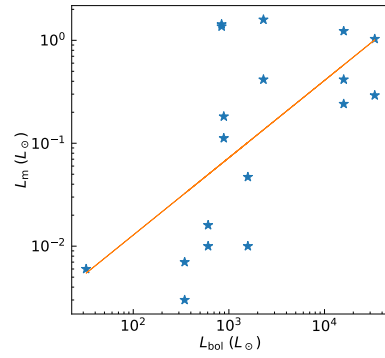
(c) HCO^+

(d) CS

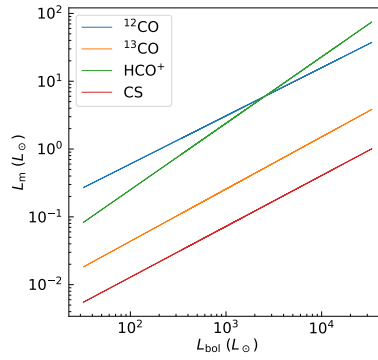


(e) Fitting lines

Figure 15. The outflow force (F) of the different molecular outflows as a function of the bolometric luminosity (L_{bol}) of each central IRAS source. The molecular line is given at the bottom of each panel. Panel (e) is the least-square fitting lines of the four molecular outflows.

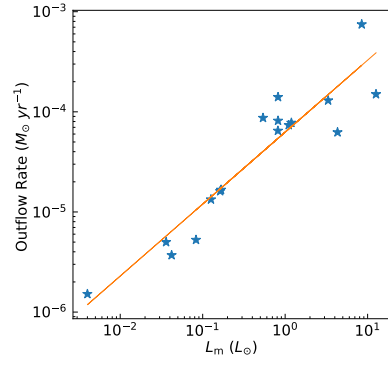
(a) ^{12}CO (b) ^{13}CO (c) HCO^+ 

(d) CS

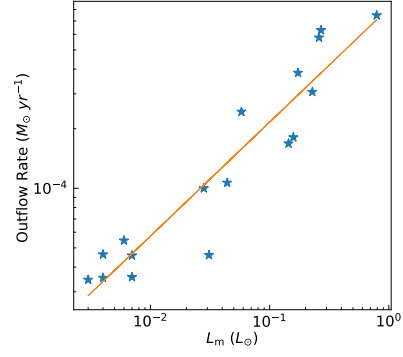


(e) Fitting lines

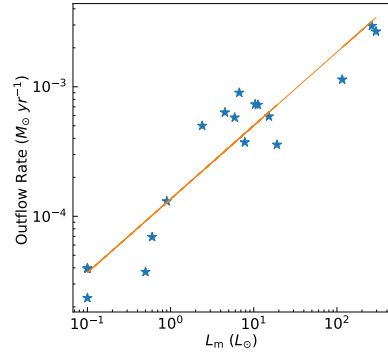
Figure 16. The mechanical luminosity (L_m) of the different molecular outflows as a function of the bolometric luminosity (L_{bol}) of the central IRAS source. The molecular line is given at the bottom of each panel. Panel (e) is the least-square fitting lines of the four molecular outflows.



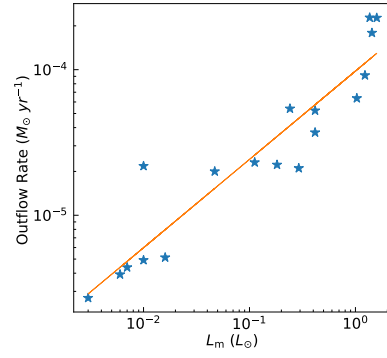
(a) ^{12}CO



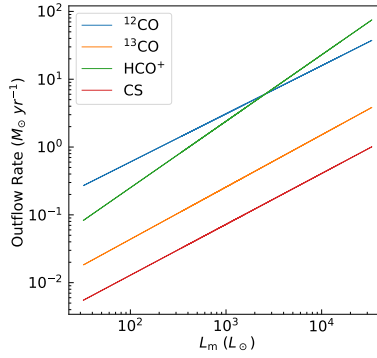
(b) ^{13}CO



(c) HCO^+



(d) CS



(e) Fitting lines

Figure 17. The outflow rate (\dot{M}) of the different molecular outflows as a function of the mechanical luminosity (L_m) of outflow. The molecular transition is given at the bottom of each panel. Panel (e) is the least-square fitting lines of the four molecular outflows.

REFERENCES

- Arce, H. G., Shepherd, D., Gueth, F., et al. 2007, in *Protostars and Planets V*, ed. B. Reipurth, D. Jewitt, & K. Keil, 245. <https://arxiv.org/abs/astro-ph/0603071>
- Bally, J. 2016, *ARA&A*, 54, 491, doi: [10.1146/annurev-astro-081915-023341](https://doi.org/10.1146/annurev-astro-081915-023341)
- Bally, J., & Lada, C. J. 1983, *ApJ*, 265, 824, doi: [10.1086/160729](https://doi.org/10.1086/160729)
- Bechis, K. P., Harvey, P. M., Campbell, M. F., & Hoffmann, W. F. 1978, *ApJ*, 226, 439, doi: [10.1086/156626](https://doi.org/10.1086/156626)
- Beltrán, M. T., Girart, J. M., & Estalella, R. 2006, *A&A*, 457, 865, doi: [10.1051/0004-6361:20065132](https://doi.org/10.1051/0004-6361:20065132)
- Beuther, H., Schilke, P., Sridharan, T. K., et al. 2002, *A&A*, 383, 892, doi: [10.1051/0004-6361:20011808](https://doi.org/10.1051/0004-6361:20011808)
- Bontemps, S., Andre, P., Terebey, S., & Cabrit, S. 1996, *A&A*, 311, 858
- Churchwell, E. 1997, *ApJL*, 479, L59, doi: [10.1086/310578](https://doi.org/10.1086/310578)
- Clark, F. O. 1986, *A&A*, 164, L19
- Edwards, S., & Snell, R. L. 1983, *ApJ*, 270, 605, doi: [10.1086/161152](https://doi.org/10.1086/161152)
- Fuente, A., Neri, R., Martín-Pintado, J., et al. 2001, *A&A*, 366, 873, doi: [10.1051/0004-6361:20000358](https://doi.org/10.1051/0004-6361:20000358)
- Fukui, Y. 1989, in *European Southern Observatory Conference and Workshop Proceedings*, Vol. 33, European Southern Observatory Conference and Workshop Proceedings, 95–117
- Garden, R. P., Hayashi, M., Gatley, I., Hasegawa, T., & Kaifu, N. 1991, *ApJ*, 374, 540, doi: [10.1086/170143](https://doi.org/10.1086/170143)
- Harju, J., Lehtinen, K., Booth, R. S., & Zinchenko, I. 1998, *A&AS*, 132, 211, doi: [10.1051/aas:1998448](https://doi.org/10.1051/aas:1998448)
- Hirota, T., Ando, K., Bushimata, T., et al. 2008, *PASJ*, 60, 961, doi: [10.1093/pasj/60.5.961](https://doi.org/10.1093/pasj/60.5.961)
- Ho, P. T. P., Moran, J. M., & Rodriguez, L. F. 1982, *ApJ*, 262, 619, doi: [10.1086/160454](https://doi.org/10.1086/160454)
- Kamezaki, T., Imura, K., Omodaka, T., et al. 2014, *ApJS*, 211, 18, doi: [10.1088/0067-0049/211/2/18](https://doi.org/10.1088/0067-0049/211/2/18)
- Kennicutt, R. C., & Evans, N. J. 2012, *ARA&A*, 50, 531, doi: [10.1146/annurev-astro-081811-125610](https://doi.org/10.1146/annurev-astro-081811-125610)
- Kwan, J., & Scoville, N. 1976, *ApJL*, 210, L39, doi: [10.1086/182298](https://doi.org/10.1086/182298)
- Li, F. C., Xu, Y., Wu, Y. W., et al. 2016, *AJ*, 152, 92, doi: [10.3847/0004-6256/152/4/92](https://doi.org/10.3847/0004-6256/152/4/92)
- Li, Q., Zhou, J., Esimbek, J., et al. 2019, *MNRAS*, 488, 4638, doi: [10.1093/mnras/stz2044](https://doi.org/10.1093/mnras/stz2044)
- Li, Y., Li, F.-C., Xu, Y., et al. 2018, *ApJS*, 235, 15, doi: [10.3847/1538-4365/aaab67](https://doi.org/10.3847/1538-4365/aaab67)
- Liu, M., Tan, J. C., De Buizer, J. M., et al. 2020, arXiv e-prints, arXiv:2006.06424. <https://arxiv.org/abs/2006.06424>
- Margulis, M., Lada, C. J., & Snell, R. L. 1988, *ApJ*, 333, 316, doi: [10.1086/166748](https://doi.org/10.1086/166748)
- Maud, L. T., Moore, T. J. T., Lumsden, S. L., et al. 2015, *MNRAS*, 453, 645, doi: [10.1093/mnras/stv1635](https://doi.org/10.1093/mnras/stv1635)
- McKee, C. F., & Ostriker, E. C. 2007, *ARA&A*, 45, 565, doi: [10.1146/annurev.astro.45.051806.110602](https://doi.org/10.1146/annurev.astro.45.051806.110602)
- Meyers-Rice, B. A., & Lada, C. J. 1991, *ApJ*, 368, 445, doi: [10.1086/169709](https://doi.org/10.1086/169709)
- Moscadelli, L., Reid, M. J., Menten, K. M., et al. 2009, *ApJ*, 693, 406, doi: [10.1088/0004-637X/693/1/406](https://doi.org/10.1088/0004-637X/693/1/406)
- Narayanan, G., & Walker, C. K. 1996, *ApJ*, 466, 844, doi: [10.1086/177559](https://doi.org/10.1086/177559)
- Plume, R., Jaffe, D. T., & Evans, Neal J., I. 1992, *ApJS*, 78, 505, doi: [10.1086/191636](https://doi.org/10.1086/191636)
- Reid, M. J., Menten, K. M., Brunthaler, A., et al. 2019, *ApJ*, 885, 131, doi: [10.3847/1538-4357/ab4a11](https://doi.org/10.3847/1538-4357/ab4a11)
- Rodriguez, L. F., Ho, P. T. P., & Moran, J. M. 1980, *ApJL*, 240, L149, doi: [10.1086/183342](https://doi.org/10.1086/183342)
- Rygl, K. L. J., Brunthaler, A., Reid, M. J., et al. 2010, *A&A*, 511, A2, doi: [10.1051/0004-6361/200913135](https://doi.org/10.1051/0004-6361/200913135)
- Sanders, D. B., & Mirabel, I. F. 1996, *ARA&A*, 34, 749, doi: [10.1146/annurev.astro.34.1.749](https://doi.org/10.1146/annurev.astro.34.1.749)
- Schreyer, K., Helmich, F. P., van Dishoeck, E. F., & Henning, T. 1997, *A&A*, 326, 347
- Shan, W., Yang, J., Shi, S., et al. 2012, *IEEE Transactions on Terahertz Science and Technology*, 2, 593, doi: [10.1109/TTHZ.2012.2213818](https://doi.org/10.1109/TTHZ.2012.2213818)
- Shepherd, D. S., & Churchwell, E. 1996, *ApJ*, 457, 267, doi: [10.1086/176727](https://doi.org/10.1086/176727)
- Shu, F. H., Adams, F. C., & Lizano, S. 1987, *ARA&A*, 25, 23, doi: [10.1146/annurev.aa.25.090187.000323](https://doi.org/10.1146/annurev.aa.25.090187.000323)
- Snell, R. L., Dickman, R. L., & Huang, Y. L. 1990, *ApJ*, 352, 139, doi: [10.1086/168521](https://doi.org/10.1086/168521)
- Snell, R. L., Huang, Y. L., Dickman, R. L., & Claussen, M. J. 1988, *ApJ*, 325, 853, doi: [10.1086/166056](https://doi.org/10.1086/166056)
- Snell, R. L., Scoville, N. Z., Sanders, D. B., & Erickson, N. R. 1984, *ApJ*, 284, 176, doi: [10.1086/162397](https://doi.org/10.1086/162397)
- Sugitani, K., Fukui, Y., Mizuni, A., & Ohashi, N. 1989, *ApJL*, 342, L87, doi: [10.1086/185491](https://doi.org/10.1086/185491)
- Tatematsu, K., Umemoto, T., Heyer, M. H., et al. 1998, *ApJS*, 118, 517, doi: [10.1086/313143](https://doi.org/10.1086/313143)
- Trinidad, M. A., Curiel, S., Torrelles, J. M., et al. 2004, *The Astrophysical Journal*, 613, 416, doi: [10.1086/422874](https://doi.org/10.1086/422874)
- Turner, B. E., Pirogov, L., & Minh, Y. C. 1997, *ApJ*, 483, 235, doi: [10.1086/304228](https://doi.org/10.1086/304228)
- Walker, R. N. F., & Masheder, M. R. W. 1997, *MNRAS*, 285, 862, doi: [10.1093/mnras/285.4.862](https://doi.org/10.1093/mnras/285.4.862)
- Wilson, T. L., Rohlfs, K., & Hüttemeister, S. 2013, *Tools of Radio Astronomy*, doi: [10.1007/978-3-642-39950-3](https://doi.org/10.1007/978-3-642-39950-3)

- Wood, D. O. S., & Churchwell, E. 1989, *ApJ*, 340, 265, doi: [10.1086/167390](https://doi.org/10.1086/167390)
- Wright, E. L., Eisenhardt, P. R. M., Mainzer, A. K., et al. 2010, *AJ*, 140, 1868, doi: [10.1088/0004-6256/140/6/1868](https://doi.org/10.1088/0004-6256/140/6/1868)
- Wu, Y., Wei, Y., Zhao, M., et al. 2004, *A&A*, 426, 503, doi: [10.1051/0004-6361:20035767](https://doi.org/10.1051/0004-6361:20035767)
- Xu, Y., Reid, M. J., Zheng, X. W., & Menten, K. M. 2006a, *Science*, 311, 54, doi: [10.1126/science.1120914](https://doi.org/10.1126/science.1120914)
- Xu, Y., Shen, Z. Q., Yang, J., et al. 2006b, *AJ*, 132, 20, doi: [10.1086/504466](https://doi.org/10.1086/504466)
- Xu, Y., Li, J. J., Reid, M. J., et al. 2013, *ApJ*, 769, 15, doi: [10.1088/0004-637X/769/1/15](https://doi.org/10.1088/0004-637X/769/1/15)
- Xu, Y., Reid, M., Dame, T., et al. 2016, *Science Advances*, 2, e1600878, doi: [10.1126/sciadv.1600878](https://doi.org/10.1126/sciadv.1600878)
- Yang, J., Umemoto, T., Iwata, T., & Fukui, Y. 1991, *ApJ*, 373, 137, doi: [10.1086/170032](https://doi.org/10.1086/170032)
- Zhang, Q., Hunter, T. R., Brand, J., et al. 2005, *ApJ*, 625, 864, doi: [10.1086/429660](https://doi.org/10.1086/429660)
- . 2001, *ApJL*, 552, L167, doi: [10.1086/320345](https://doi.org/10.1086/320345)
- Zinchenko, I., Henning, T., & Schreyer, K. 1997, *A&AS*, 124, 385, doi: [10.1051/aas:1997361](https://doi.org/10.1051/aas:1997361)